ATLAS Internal Note
CAL–NO–077
5 october 1995

Performances of the ATLAS electromagnetic calorimeter filled with liquid Krypton : Higgs mass resolution in the $H^o \rightarrow \gamma\gamma$ and $H^o \rightarrow ZZ^* \rightarrow 4\ e^{\pm}$ benchmark channels.

Gaston Parrour, Pierre Pétroff,
Laurent Serin and Vincent Tisserand
Laboratoire de l'Accélérateur Linéaire,
IN2P3-CNRS et Université Paris-Sud
91405 Orsay Cédex, France.

Abstract

This note presents the performances of the EM barrel calorimeter filled with liquid Krypton, both in energy resolution and in angular resolution with single particles. The Higgs mass is estimated with the full calorimeter in two benchmarks channels : $\gamma\gamma$ and $ZZ^* \rightarrow e^+e^-e^+e^-$, for masses of respectively $m_{H^o} = 100$ GeV/c^2 and 130 GeV/c^2. In both channels the improvement on the total mass resolution compared to the liquid Argon option is 20%.

1 Introduction

The optimization of the electromagnetic (EM) accordion barrel calorimeter filled with liquid Krypton (LKr) has been considered in parallel to the liquid Argon (LAr) main option (ref. [1]). The shorter radiation length of LKr compared to LAr (4.8 cm instead of 13.9 cm) allows to use thinner absorber plates to achieve the same total calorimeter thickness of at least 25 X_0. In consequence, the use of LKr as an active medium is very attractive because a better sampling and noise term in the energy resolution than LAr can be reached [1].

Two different geometries have been simulated. The first one (TP LKr model), already described in ref. [1] and ref. [2], is based on the same design than the LAr option. But, since the publication of the ATLAS Technical Proposal, a new Krypton geometry (new LKr model), giving a better energy resolution, has been proposed. Most of the results presented here have been obtained with this geometry, more specially the results on Higgs mass resolution.

After a description of the geometries used in the simulation, the sampling term and the angular resolution with single particles are presented, followed by a detailed analysis of the electronics and pileup noises contribution to the total energy resolution. A special care is taken on the cluster sizes optimization in view of the Higgs into $\gamma\gamma$ channel analysis. Finally, the Higgs mass total resolution is estimated, in two benchmarks channels : $\gamma\gamma$ and $ZZ^* \rightarrow e^+e^-e^+e^-$.

The simulation of the different LKr models performances has been performed with the HP system farm BASTA at CCIN2P3 Lyon.

2 Geometry description

The layout has been implemented in the general GEANT simulation DICE of the ATLAS detector, which also included a detailed description of the accordion geometry.

The full design is based on the Technical Proposal (TP) model [1], and more details can be found in ref.[2]. The basic model is the so-called "**hybrid**" model which consists in :

- a **presampler** which is an independent active layer, installed downstream the cryostat wall. The active LKr layer has a radial thickness of 10 mm. The granularity is $\Delta\phi = 0.0245 \times 4$, $\Delta\eta = 0.025/8$ at $|\eta| > 0.8$ and $\Delta\eta = 0.025$ at $|\eta| < 0.8$.

- a **calorimeter** divided in depth in three compartments (S_1, S_2 and S_3). S_1, referenced as an **integrated preshower**, is segmented in narrow strips in η direction with the same fine granularity as the **presampler** at $|\eta| > 0.8$. The granularity of the two last samplings is $\Delta\eta = 0.025$, $\Delta\phi = 0.0245$ for S_2 and a same η granularity for S_3 but a twice larger granularity in ϕ.

All dimensions, thicknesses and materials valuable both for LAr and LKr are extensively described in ref. [3]. Here we only recall the salient features concerning the LKr geometries not described elsewhere.

[1] Although the LKr option has not been chosen by the collaboration, we consider as necessary to finalize the work done on this subject by a note.

Due to shorter LKr radiation length, the corresponding material thickness in front of the calorimeter is slightly higher than in the case of LAr. To reduce the amount of inactive LKr between the calorimeter and the presampler, a "0T" electronic scheme has been adopted. Fig. 1 shows the different contributions of material upstream the calorimeter. At $\eta = 0$ the total material thickness in front of the active layer of the presampler is 1.2 X_0 and rises up to 2.5 X_0 at $\eta = 1.3$.

In order to recover the energy lost between the active part of the presampler and the active part of the calorimeter, a "massless gap" technique is used. The first fold of the absorber is equipped with light material only, covering a region of 2.5 cm in radial direction. The role of the massless gap is more crucial in LKr case than in LAr case.

In the TP LKr model the lead thickness changes at $\eta = 0.6$ to compensate for the decrease of the sampling frequency with η. The optimized lead thickness is 1.4 mm ($|\eta| < 0.6$) and 1.0 mm ($|\eta| > 0.6$). Fig. 2 shows the total thickness of the calorimeter versus η. In the new LKr model the lead thickness is not reduced at fixed η but remains constant. The 1^{rst} and 2^{nd} sampling absorbers are 1.1 mm thick while the 3^{rd} one is 1.8 mm in order to get 25 X_0 at η=0. Figure 3 shows the geometry and figure 4 gives the total radiation length in this model.

The 1^{rst} sampling is tapered with η, resulting in a constant thickness of 4.5 X_0 at all rapidities. The boundary between the 2^{nd} and 3^{rd} sampling is at fixed radius. At $|\eta| = 0.$, the thickness is 9.9 X_0 and 9.5 X_0 respectively, for TP LKr model and 12 X_0 and 8.5 X_0 respectively, for the new LKr model. In the case of this new LKr model the relative large thickness of the 2^{nd} compartment has been chosen to minimize the contribution of the 3^{rd} compartment which should have worse performances due to thicker absorber.

3 Energy resolution with single particles

3.1 Analysis procedure

The main features of the analysis procedure are the following :

- The cluster size is optimized to find a good compromise between the contribution of electronics and pileup noises and sampling term to the total Higgs mass resolution. Reduced cluster sizes are defined for unconverted γ's in the tracker. Table 1 gives the details of the clusterisation. As 50 % of pileup contribution comes from S_1 and from the presampler, the number of strips in ϕ is reduced as much as possible, according to the centroïd position in S_2 with respect to the corresponding strip in S_1 and in presampler. Note that this optimization is more important in the case of LKr compared to LAr, because the sampling term contribution is much closer to the other ones (see figure 5, values of the sampling term contribution are explained in next chapter).

  For $H^o \rightarrow ZZ^* \rightarrow 4\ e^{\pm}$ analysis a 3×7 cluster is used only (24×2 strips in S_1).

- A correction of collected energy versus the impact point in the η direction is applied (figure 6).

- A correction of the variation of the calorimeter response in ϕ is also performed. Thanks to the "N=4" overlap of folds in the accordion, the amplitude of the modulation is only 0.5 % peak-to-peak and 0.3 % r.m.s, before correction (figure 7).

$\Delta\eta \times \Delta\phi$	presampler	samp. 1	samp. 2 and 3
converted γ			
barrel	8×2 strips or 1 cell ×2 strips for $\|\eta\| < 0.8$	24×2 strips	3×7 cells
endcap	none	24×2 strips	3×7 cells
unconverted γ			
barrel	8×2 (1) strips or 1 cell ×2 (1) strips for $\|\eta\| < 0.8$	16×2 (1) strips	3×5 cells
endcap	none	16×2 (1) strips	3×5 cells

Table 1: *size of clusters used for energy reconstruction of photons. converted* γ *means photon converted in material of inner tracker with* $R_{conv} < 90$ *cm and tagged from "kine bank".*

- A set of calibration coefficients are calculated with the Minuit programme, from single γ's 50 GeV E_T at differents rapidities, by minimizing the energy resolution.

  In the new LKr model case, a weight of 1.48 is applied to the 3^{rd} sampling response. This value has been determined after an iterative procedure with single γ's of 50 GeV and 200 GeV E_T at η=0.3. Then this value has been kept constant for each cluster sizes, η position and incident energy.

  Weights are applied on the presampler and the 1^{rst} calorimeter compartment. A global normalisation is also determined to recover the incident energy in average. These coefficients vary with rapidity but not with energy. Three different calibrations have been calculated : one for 3×7 clusters (all γ's, electrons), one for converted γ's and the last one for unconverted γ's.

3.2 Sampling term contribution

Assuming that the inner tracker has a full efficiency to tag the converted photons, the distinction between converted and unconverted photons has been made for the Higgs mass in $\gamma\gamma$ analysis. According to table 1, Fig. 8 shows the sampling term obtained with optimized cluster sizes for the analysis of $H^o \rightarrow \gamma\gamma$. Even if a systematic deterioration is observed on the sampling term compared to a 3×7 cluster, the total resolution on Higgs mass will be improved at last (around 25 % $\gamma\gamma$ pairs only have at least one γ converted in tracker). At $\eta < 0.8$ the sampling term varies like $1/\sqrt{sin\theta}$ as expected. At higher η values, the deviation from the $1/\sqrt{sin\theta}$ dependance of the sampling term comes from the contribution of the material in front of the presampler. This contribution ranges from 1.7 % to 3.9 % [2], when η varies from 0.9 to 1.3. The presampler cannot recover completly for the energy lost. It is clear that having less material (for example the coil downstream the calorimeter) the LKr option should be much more attractive.

[2] calculated by a quadratic substraction of the expected sampling term (scaled as $1/\sqrt{sin\theta}$) to the measured sampling term.

Fig. 9 shows the sampling term resolution with two different set of calibration coefficients for 50 GeV E_T corresponding to converted or unconverted photons in the inner tracker. A slight improvement is observed at high η values.

To check the "robustness" of the performances, the figure 10 compares the sampling term with two LKr clearance thicknesses in front of the presampler, 1 cm and 2 cm respectively. The effect of increasing thickness clearance is only slightly sensitive at high η values.

In order to estimate the intrinsic performance of the new LKr model, γ's of different energies have been generated at η= 0.3. This low η value corresponds to a region where the contribution of material is small and well understood. The resolution is displayed in figure 11 and has been parametrized by a sampling term plus a constant term :

$$\frac{\sigma(E)}{E}(\%) \;=\; \frac{(6.04 \pm .12)}{\sqrt{E}} \oplus (.24 \pm .02)$$

Fig. 12 shows a comparison between the TP LKr model and new LKr model sampling terms, with photons of 50 GeV E_T. The difference of effective lead thickness (1.4 mm compared to 1.1 mm) explains the better resolution at low η of the new LKr model.

By comparison, the sampling term with LAr TP model (ref. [2]) is plotted also in figure 13. The gain in resolution with LKr is obvious at low η values.

For the $H^o \rightarrow ZZ^* \rightarrow 4\ e^{\pm}$ channel sampling term for electrons of low transverse energy has been evaluated (average P_T value for softer electrons is around 15 GeV/c for m_{H^o}= 130 GeV/c^2). In fig. 14 the sampling term for electrons of P_T = 10 GeV is displayed, and, if one compares with the resolution in the LAr case, ref. [2], a net gain appears at low rapidity.

Longitudinal shower leakage can deteriorate the sampling term resolution [3] (ref [2]). Fig. 15 shows a good energy resolution of 0.35 % for electrons of E_T = 500 GeV at η = 0.3.

The performance of the new LKr model geometry has also been studied when LKr is replaced by LAr. The total thickness is reduced from 26.5 X_0 to 22.5 X_0 at η=0. Fig. 15 shows that a resolution of 0.50 % can be reached by adding the properly weighted energy of the first hadronic compartment. A threshold of 1 GeV is set on the leakage energy, which corresponds to roughly 2 σ above the electronic noise in the first hadronic compartment, (see fig. 16). Expected performances at lower energies have also been simulated. With γ's of E_T= 50 GeV the sampling term is $(9.0 \pm .2)\%.(GeV)^{1/2}$ at η= 0. and $(11.9 \pm .3)\%.(GeV)^{1/2}$ at η= 1.3. At low rapidity one would have expected better value because of the lead plates thickness (1.1 mm lead plates in the 1^{rst} and 2^{nd} sampling of the calorimeter instead of 1.8 mm in case of TP LAr model), but the benefit is poored by longitudinal leakage and the energy deposited in the hadronic calorimeter is too low to be recovered.

3.3 Pileup, electronics noise and constant term contributions

According to ref. [1] the total ENI[4] is a factor 1.6 smaller in LKr than in LAr. This gives the opportunity of designing a geometry with a "0T" readout scheme in the 1^{rst}

[3] The error on pair production cross-section in GEANT has been corrected for this simulation.

[4] Equivalent Noise Intensity.

$\|\eta\|$	presampler	samp. 1	samp. 2 and 3	electronics	pileup
[0.,0.5]	8×2	24×2	3×7	180.	338.
[0.5,1.4]	8×2	24×2	3×7	180.	287.
[1.4,2.4]	none	24×2	3×7	-306.×($\|\eta\|$-1.4)+534.	275.
[2.4,3.2]	none	24×2	3×7	-142.5×($\|\eta\|$-2.4)+228.	275.
[0.,0.5]	8×2	16×2	3×5	156.	278.
[0.5,1.4]	8×2	16×2	3×5	156.	247.
[0.,0.5]	8×1	16×2	3×5	151.	270.
[0.5,1.4]	8×1	16×2	3×5	151.	240.
[0.,0.5]	8×2	16×1	3×5	149.	242.
[0.5,1.4]	8×2	16×1	3×5	149.	215.
[0.,0.5]	8×1	16×1	3×5	143.	234.
[0.5,1.4]	8×1	16×1	3×5	143.	208.
[1.4,2.4]	none	16×2	3×5	-259.×($\|\eta\|$-1.4)+452.	202.
[2.4,3.2]	none	16×2	3×5	-121.×($\|\eta\|$-2.4)+193.	202.
[1.4,2.4]	none	16×1	3×5	-259.×($\|\eta\|$-1.4)+452.	173.
[2.4,3.2]	none	16×1	3×5	-121.×($\|\eta\|$-2.4)+193.	173.

Table 2: *electronics noise and pileup noise expressed as MeV/sin(θ) (except for electronics noise in endcap (MeV)), for different regions in η and different cluster sizes.*

compartment of the calorimeter. The price to pay is a bigger electronics noise contribution (especially coherent noise and higher sensitivity to cross-talk). The advantage is to minimize the amount of inactive liquid between the presampler and the calorimeter.

The optimization of the cluster sizes, according to table 1, allows to reduce the electronics and pileup noises contributions, by a factor 1.18 (roughly estimated by $\sqrt{\frac{3\times7}{3\times5}}$). This reduction is apply to unconverted γ's (85 % of all γ's).

In order to be at the optimum shaping response, electronics noise was rescaled from 40 ns to 36 ns peaking time $t_p(\delta)$ (response from 5 to 100 %), according to ref. [4] [5]. Pileup contribution have been recalculated since ref. [5], for all cluster sizes choosen and for this new peaking time (the data used are those of ref. [5]).

Table 2 gives in details the pileup and electronics noise contributions according to different cluster sizes. The pileup and electronics noise contributions to the electron energy resolution are estimated for a 3×7 cluster.

The constant term contribution of 0.7 % quoted in TP and extracted from ref. [6] is kept, both for barrel and endcap. This number is slightly pessimistic in barrel part, because one should expect a 0.4 % contribution from module to module and 0.4 % from cell to cell [7], leading to a value of 0.55 % . For the endcap part this number is perhaps a little bit optimistic, as result of test beam is around 0.9 % over a large area ([8]).

[5] ENI is estimated as quadratic sum of serie noise that scales as $\frac{1}{t^{3/2}}$ and parallel noise that scales as $\frac{1}{t^{1/2}}$. Initial noise for $t_p(\delta)$ = 40 ns in strips of 1rst calorimeter compartment has been changed from 14 MeV to 20 MeV, in order to accomodate to "0T" choice.

4 Angular resolution

The angular resolution has been simulated with γ's of 50 GeV E_T. The η value is choosen randomly around a fixed η value over a range of $\pm$ 1 η cell in the 2 nd sampling. The ϕ value is choosen randomly over 2π. The vertex position is smeared with a σ of 5.6 cm in the z direction.

The best accuracy is obtained by taking three strips ($\pm$ 1 around the most energetics) both in fine grained part of the presampler ($\eta > 0.8$) and in the 1^{rst} sampling. The 2^{nd} and 3^{rd} samplings responses are added (clusters 3×3) in order to increase the lever arm between the presampler or the 1^{rst} sampling and the 2^{nd}+3^{rd} samplings ([9]).

Typical "S-shape" corrections have been applied to measure the η position in the calorimeter (fig. 17 and 18).

At $\eta > 0.8$, the presampler is used when the signal deposited corresponds to at least two mips.

The results are presented in figure 19. The resolution ranges from 60 mrad $/\sqrt{E}$ to 65 mrad $/\sqrt{E}$ for η between 0.3 and 1.3, with the calorimeter alone. When the part of the presampler with fine grained granularity ($\eta > 0.8$) is used the resolution drops to around 40 mrad (presampler allows longer lever arms by a factor of ~ 2).

The resolution on the z-vertex position is shown in figure 20, in which presampler is used when it is possible.

5 Higgs in two gammas

About three thousand events of $H^o \rightarrow \gamma\gamma$ have been fully simulated in the detector (tracker + calorimeters), with the new LKr model.

They have been generated at m_{H^o}= 100 GeV/c^2 from the direct processes, gluon-gluon fusion and WW, ZZ fusion, with M_{top}= 170 GeV/c^2 and PYTHIA 5.7 default structure fonctions. A prefiltering has been done requiring γ's with $E_T > 20$ GeV and $|\eta| < 2.7$. This prefiltering corresponds to a signal efficiency of 60 %.

5.1 Study of the resolution

The calorimeter response has been fully used for energy and angular reconstruction of the 2 γ's. Converted and unconverted γ's have been considered separately. These γ's have been tagged with "kine bank" if transverse radius of conversion, R_{conv} is <90 cm [6]. In the next future, a tagging of converted γ's using the tracker reconstruction will be implemented.

In figure 21, one can see the ratio of reconstructed energy to incident energy versus η. This curve, obtained with photons from $H^o \rightarrow \gamma\gamma$ gives an estimation of the uniformity of the detector response. At higher rapidity, in the endcap region, slopes due to lateral leakage have been corrected for. They appear because the calibration has been performed with single γ's samples at three η positions only: 1.7 , 2.0 and 2.4.

In figure 21, one can also see the response in the transition region between the barrel and the endcap calorimeters. At η=0., the hole is due to an overestimate, in the

[6] according to inner tracker experts 90 cm is the maximum radius value to search converted γ's as it is necessary to keep enough radius in TRT to fit electrons tracks.

simulation, of the material separating the two half parts of the barrel (5. cm of steel instead of $\sim$ 0.5 cm of LKr). These two regions $1.375 < |\eta| < 1.525$ and $|\eta| < 0.05$ have not been used for final analysis, resulting in two fiducial cuts. For the last one, a relative efficiency of 95 % for $\gamma\gamma$ pairs is obtained. These cuts have been also applied to the $H^o \rightarrow ZZ^* \rightarrow 4\ e^{\pm}$ analysis.

Additional cuts extracted from ref. [10] and ref. [11] have been used :

- a cut on energy leakage behind the EM calorimeter is applied, used for rejection against jets. Typically less of 500 MeV E_T is required in the first hadronic compartment.
- an isolation cut on transverse shower profile is set : $\frac{(E^{7\times7}_{samp2.} - E^{3\times5}_{samp2.})}{E^{3\times5}_{samp2.}}$, which is required to be typically less than 10 %.
- against π^o faking a high transerve energy γ, a profile cut is applied. In the 1^{rst} sampling (S_1), around the strip of maximum energy, 2 quantities are computed :

$$E_1 = \sum_{i=max.-1}^{max.+1} E_i \ \text{ and } \ E_2 = \sum_{i=max.-15}^{max.+15} E_i$$

The ratio E_1/E_2 has to be typically bigger than 50 %.

An efficiency of $\varepsilon_\gamma \simeq 80$ % is obtained after these three cuts. It does not depend on the liquid neither if γ's convert or not in the inner tracker.

The usual kinematics cuts have been also applied to reduce the irreductible $\gamma\gamma$ background. It is required that the 2 γ's are in $|\eta| \leq 2.5$, one γ has $P_T > 40$ GeV/c and the other has $P_T > 25$ GeV/c, and $P_T^1 \ / \ (P_T^1 + P_T^2) < 0.7$.

Finally, the total acceptance of two γ's from Higgs decay is $\varepsilon_\gamma \simeq 25.7$ % (40.5 % from fiducial and kinematics cuts and 63.4 % from prefiltering).

The 2 γ's sampling term is presented in figure 22 and figure 23, for a barrel-barrel configuration and all possible configurations respectively. Calibrations and corrections of the modulations in the calorimeter are taken from 50 GeV E_T single γ's simulation.

The resolution quoted in figure 22 (σ=7.3 %.$(GeV)^{1/2}$) is in a good agreement with average value obtained with the distribution (open triangles) of figure 8, where the mean value of the sampling term in barrel part is around 7.5 %.$(GeV)^{1/2}$ (distribution of γ's is flat with rapidity).

The fitted vertex from the 2 γ's and vertex diamond are combined with proper weights. These weights have been obtained with the γ's of the angular resolution study, "S-shapes" parametrized have also been corrected. Then, each γ angle is calculated. If the γ converts very soon, active tracker z-layers are used, taking into account the tracker performances. The very long lever arm for pointing allows to improve by 5 % the angular contribution to the total Higgs mass resolution. In the barrel-endcap configuration of $\gamma\gamma$ pairs, it has been checked that the vertex accuracy is dominated by the γ in barrel, as expected. While, in the endcap-endcap configuration, the z vertex position is essentially given by the vertex diamond.

Figures 24 and 25 show the spectra of all contributions to total mass resolution for all γ's of the H^o. Note that the distribution of the angular contribution to the total mass

$\gamma\gamma$ configuration	all γ's	Barrel-Barrel	Barrel-Endcap	Endcap-Endcap
number of events	1145	550	360	235
samp. term (corr.)	687 $\pm$ 17	673 $\pm$ 24	690 $\pm$ 41	637 $\pm$ 46
el. noise + pileup	389 $\pm$ 19	438 $\pm$ 15	411 $\pm$ 24	315 $\pm$ 3
el. noise + pileup + cst. term	635 $\pm$ 15	658 $\pm$ 21	640 $\pm$ 80	582 $\pm$ 56
energy resolution	939 $\pm$ 23	897 $\pm$ 35	949 $\pm$ 125	928 $\pm$ 51
angles	403 $\pm$ 21	223 $\pm$ 11	530 $\pm$ 36	943 $\pm$ 78
$\sigma_{m_{H^o}}$ fit $\pm$ 2 σ	1040 $\pm$ 30	974 $\pm$ 61	1164 $\pm$ 78	1400 $\pm$ 170 (stat.)

Table 3: *details for all individual contributions to $\sigma_{m_{H^o}}$ at high luminosity (10^{34} $cm^{-2}s^{-1}$), in unit MeV/c^2 and for $m_{H^o} = 100$ GeV/c^2.*

resolution is not gaussian. This is due to a mixing of different γ's samples, for instance, the angular resolution is bad when both γ's are measured in the endcap.

2829 events have been fully reconstructed resulting in 1145 survivals after cuts. All the contributions to total mass resolution are given in table 3 in all γ's configurations.

Table 4 and figure 26 give a comparison of the expected calorimeter performances in the cases of high luminosity 10^{34} $cm^{-2}s^{-1}$and low luminosity 10^{33} $cm^{-2}s^{-1}$.

At high luminosity, a cut at $\sim \pm 1.4$ σ in the distribution of figure 27 gives a reconstruction efficiency of ε= 80.7 %, resulting in a value of 3.08 GeV/c^2 for the mass bin. One should expect ε= 83.8 % efficiency for a perfect gaussian distribution. This 3.1 % deviation is due to a small tail contribution, as it can be checked on figures 26 and 27, corresponding to $\simeq \pm 2$ σ fit and total fit respectively.

At low luminosity, some contributions to the total resolution are reduced or supressed. The z vertex position is much better reconstructed using tracking information, since there are in average only ~ 2 interactions per crossing, and one can usually identify the Higgs vertex source [12]. Pileup and electronics noises can be reduced by adjusting the shaping response to optimum peaking time (the pileup contribution is $1/\sqrt{10}$ times the value at high luminosity). Note that the same cluster sizes optimization has been kept which worsened the sampling term in the low luminosity case.

5.2 Discussion on the results and statistical significance

The statistical significance, $S/\sqrt{B}$, has been computed following ref [13]. $H^o \rightarrow \gamma\gamma$ events produced in associated production (WH, ZH and $t\bar{t}H$, $b\bar{b}H$) have been added to the direct production. The signal cross section is enhanced but background remains the same as the events are studied in an inclusive way. At m_{H^o}= 100 GeV/c^2, this causes a 12% benefit in $S/\sqrt{B}$.

Following the table 4, the $S/\sqrt{B}$ is 5 σ at high luminosity and 3.45 σ at low luminosity. Starting from m_{H^o}= 100 GeV/c^2 results, figures 28 and 29, show the variation of the statistical significance versus the Higgs mass. The 5 σ discovery limit is already reached at m_{H^o}= 100 GeV/c^2, in the high luminosity case, and for $m_{H^o} \simeq 120$ GeV/c^2

Luminosity	10^{34} cm^{-2}s^{-1}	3.10^{33} cm^{-2}s^{-1}
sampling term (corrected)	690	690
constant term	490	490
pileup + noise	390	165
angles	400	70
$\sigma_{m_{H^o}}$ fit $\pm$ 2 σ	1040	890
$\int \mathcal{L}.dt$	10^5 pb^{-1}	3 10^4 pb^{-1}
Mass Bin ε = 80.7 %	3.08 GeV/c^2	2.49 GeV/c^2
$S/\sqrt{B}$	5.0	3.45

Table 4: *individual contributions to $\sigma_{m_{H^o}}$ for m_{H^o} = 100 GeV/c^2 at low and high luminosity (Mass Bins and corresponding statistical significances are also presented). Individual contributions to total mass resolution and total mass resolution are given in MeV/c^2.*

at low luminosity.

A comparison between LKr and LAr options can be made, using numbers presented in ref [13]. The total mass resolution improvment with LKr compared to LAr is 20% (1.04 GeV/c^2 compared to 1.25 GeV/c^2).

With the same cut at $\sim \pm$ 1.4 σ (efficiency of 80.7%), the mass bin is 3.43 GeV/c^2 with the LAr option. The relative gain in $S/\sqrt{B}$ with LKr option, becomes 7 %, mainly because the statistical significance varies like the root of the mass bin.

Following the ref. [14] the ATLAS discovery potential of the H$^o \rightarrow \gamma\gamma$ with LKr is compared to the CMS expected performances. Figures 30 and 31 give the expected $S/\sqrt{B}$ in both experiments for one year at high luminosity and for three years at low luminosity respectively. The discovery potential of the H$^o \rightarrow \gamma\gamma$ is the same at high $\mathcal{L}$ and 12 % worse only for ATLAS at low $\mathcal{L}$. Note that ATLAS results include a full simulation of the detector and a full reconstruction of γ's.

6 Higgs in four electrons

As already shown in figure 14, the use of LKr as active liquid gives clear improvement of the sampling term for electron. In order to study the effect on the Higgs mass resolution, a sample of about 3000 events was fully simulated with the new LKr model.

6.1 mass reconstruction

As the events were generated including inner bremstrahlung with the PHOTOS package [15], in order to compare the results with the ATLAS TP, they have been classified in two categories :

- Events with no inner photon or with photon such that the energy taken away is less than 0.1 % of the initial electron energy (called $N_\gamma = 0$). This corresponds to 40 % of the events.
- All events.

The kinematical cuts used were the ones already described in the ATLAS TP :

- Four leptons with $P_T > 7$ GeV/c and $|\eta| < 2.5$
- At least two leptons with $P_T > 20$ GeV/c
- One dilepton mass within $\pm$ 6 GeV/c^2 of the nominal Z^o mass and the second dilepton mass greater than 20 GeV/c^2.

Moreover two additional cuts already described in the $H^o \rightarrow \gamma\gamma$ analysis were applied to reject events with one lepton in the so called "flange" at $\eta = 0$ or in the barrel/endcap transition.

The events were reconstructed with a 3×7 cluster (24×2 in presampler and sampling S_1) calibrated with 50 GeV photons in the LKr model (performances for 10 GeV electrons are displayed in figure 14). Small improvement on noise and pileup term could be obtained by reducing the cluster size in the preshower independently of the active liquid. Parametrizations were determined and applied to correct for residual slopes versus η (fixed point calibration and energy containment in finite cluster size) and lateral η leakage in the endcap only (parabola). Attempts were done to correct for parabola in the barrel and the expected ϕ modulation but no improvement was observed.

The noise term in the endcap was defined in table 2. For the barrel taking into account the use of 24×2 cluster in the presampler, the noise term is 200 MeV/sin(θ) in LKr. Pileup numbers which were used are summarized in table 5.

Pseudo-rapidity range	Pileup in MeV
$\|\eta\| < 0.5$	344 / sin(θ)
$0.5 < \|\eta\| < 1.4$	292 / sin(θ)
$1.4 < \|\eta\| < 2.4$	274 / sin(θ)

Table 5: *Pileup r.m.s as a function of η used in four electrons analysis.*

A conservative value of 0.7 % was included for the overall constant term. All invariant masses were reconstructed without using tracker angle information but "kine banks" information.

6.2 Mass resolution results

The mass resolution including only the sampling term contribution is shown in figure 32 for LKr. A few comments can be extracted from these plots :

- In the case $N_\gamma = 0$, the mass resolution is obviously better using only barrel events. Moreover including endcap, low mass tails appear : they are explained by the presence of at least one electron hitting the calorimeter in the region $1.5 < |\eta| < 1.8$ where the inner detector amount of material is the highest.
- The effect of inner bremstrahlung gives a deterioration of about 11 % on the mass resolution, nevertheless efficiency can be maintained at the level of 80 % in the mass bin.

- As no effort was done to try to recover the photon when it is energetic (> 5 GeV), there is some room to improve the efficiency of the mass bin.

The results including the constant term, then the electronic noise and finally the pileup noise are summarized in figure 33. The mass distribution at low and high luminosity is displayed in figure 34 as an example. The relevant numbers are summarized in table 6.

(GeV/c^2)	Low luminosity	High luminosity
Krypton barrel	1.28 ± 0.05	1.46 ± 0.08
Krypton barrel + endcap	1.38 ± 0.04	1.56 ± 0.06

Table 6: *Mass resolution at low and high luminosity (fit between (127-133) GeV/c^2).*

The intrinsic improvement of LKr on mass resolution is around 30 % (barrel events) with respect to LAr TP model [16]. Meanwhile in the ATLAS framework with the LAr endcap it results only in a 20 % improvement on the mass whatever is the luminosity. As the electrons represents 50 % of the Higgs into four lepton channel, the overall four lepton mass resolution is better only by 10 % leading to a gain on statistical significance about 5 %.

7 conclusion

A full study of the ATLAS EM calorimeter capability to discover the Higgs at low mass values with LKr has been performed. In the two considered benchmark channels the improvement in mass resolution is $\sim 20\%$ compared to the LAr option. From the Higgs search point of view, the gain was considered not overwhelming compared to the total "cost" of the LKr option. Nevertheless, it is not ruled out, that energy resolution could be a crucial parameter for unexpected physics.

References

[1] ATLAS Collaboration, Technical Proposal, CERN/LHCC/94-43.

[2] F. Gianotti et al., Simulation and optimization of ATLAS EM calo : energy resolution studies, ATLAS Internal Note CAL-No-70.

[3] M. Nessi et al., Status of the ATLAS calorimetry simulation for the TP in DICE, ATLAS Internal Note SOFT-No-16.

[4] C. de la Taille et al., A fast monolithic shaper for the ATLAS EM calorimeter, ATLAS Internal Note LARG-No-10.

[5] L. Serin and V. Tisserand, Study of pileup in the ATLAS EM calorimeter, ATLAS Internal Note CAL-No-73.

[6] RD3 collaboration, Performance of a liquid argon prototype of the ATLAS accordion EM calorimeter, CERN PPE 9535(1995), submitted to NIM.

[7] L. Serin, ATLAS Internal Note in preparation.

[8] A. Chekhtman et al., Performance of a liquid argon EM endcap calorimeter using an accordion geometry, ATLAS Internal Note CAL-No-68.

[9] M. Seman et al., An optimized ATLAS EM calorimeter without a presampler, ATLAS Internal Note CAL-No-74

[10] J. Schwindling et al., simulation and optimization of the ATLAS EM calo : γ/π^o separation, ATLAS Internal Note CAL-No-72.

[11] F. Gianotti and I. Vichou, Study of $\gamma/jets$ separation with the ATLAS detector, ATLAS Internal Note in preparation.

[12] Ren-yuan Zhu and Hiro Yamamoto, Intermediate H^o searches with GEM detector, Note GEM TN-92-126.

[13] D. Froidevaux et al., MSM and MSSM Higgs rates and background in ATLAS, ATLAS Internal Note PHYS-No-048.

[14] F. Gianotti et al., Comparison of the ATLAS and CMS discovery potential for the $H^o \rightarrow \gamma\gamma$ channel at LHC, ATLAS Internal Note PHYS-No-64.

[15] E. Barberio, B. van Eijk and Z. Was, Comp. Phys. Comm. 66(1991) 115.

[16] L. Poggioli, L. Serin, presented at LArg EM optimization and simulation meeting (16 may 1995).

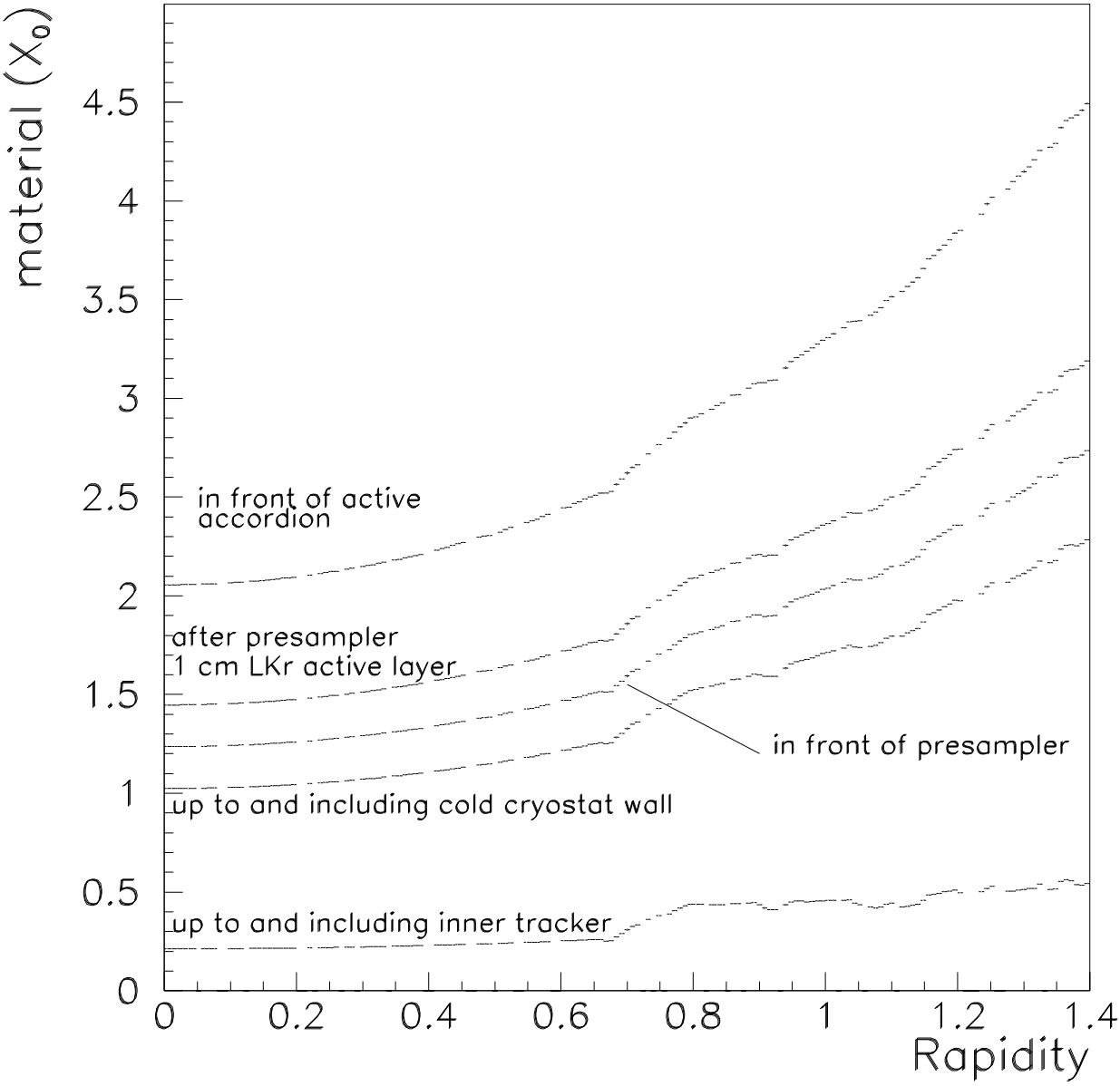

Figure 1: material distibution in front of the preshower active layer and in front of the calorimeter (number of X_0 versus η). From bottom to top : inner tracking, dead Kr layer, start of active presampler, end of active presampler, start of accordion.

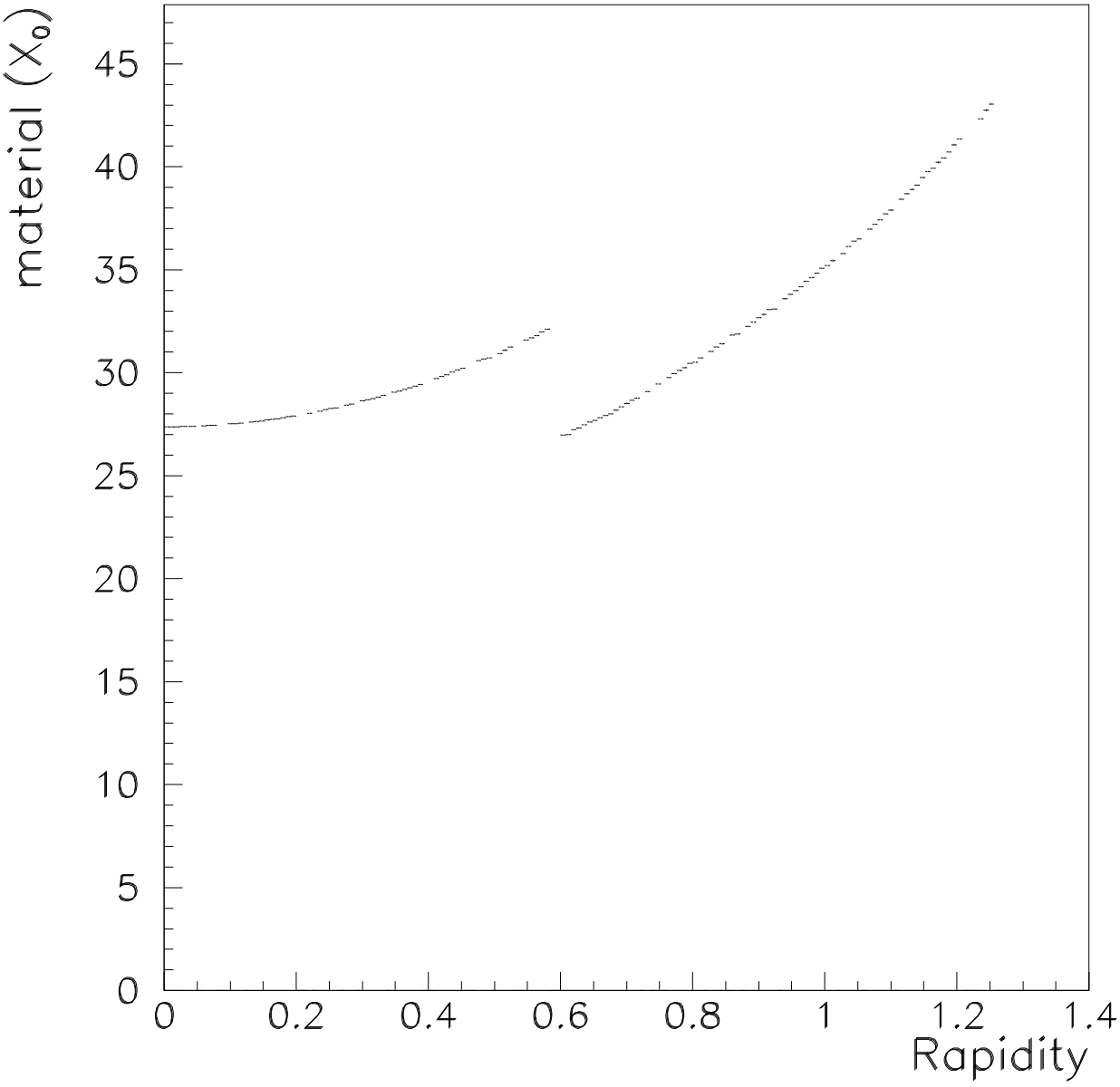

Figure 2: total radiation length after the calorimeter in TP model, with lead thickness changing at $\eta = 0.6$ (number of X_0 versus η).

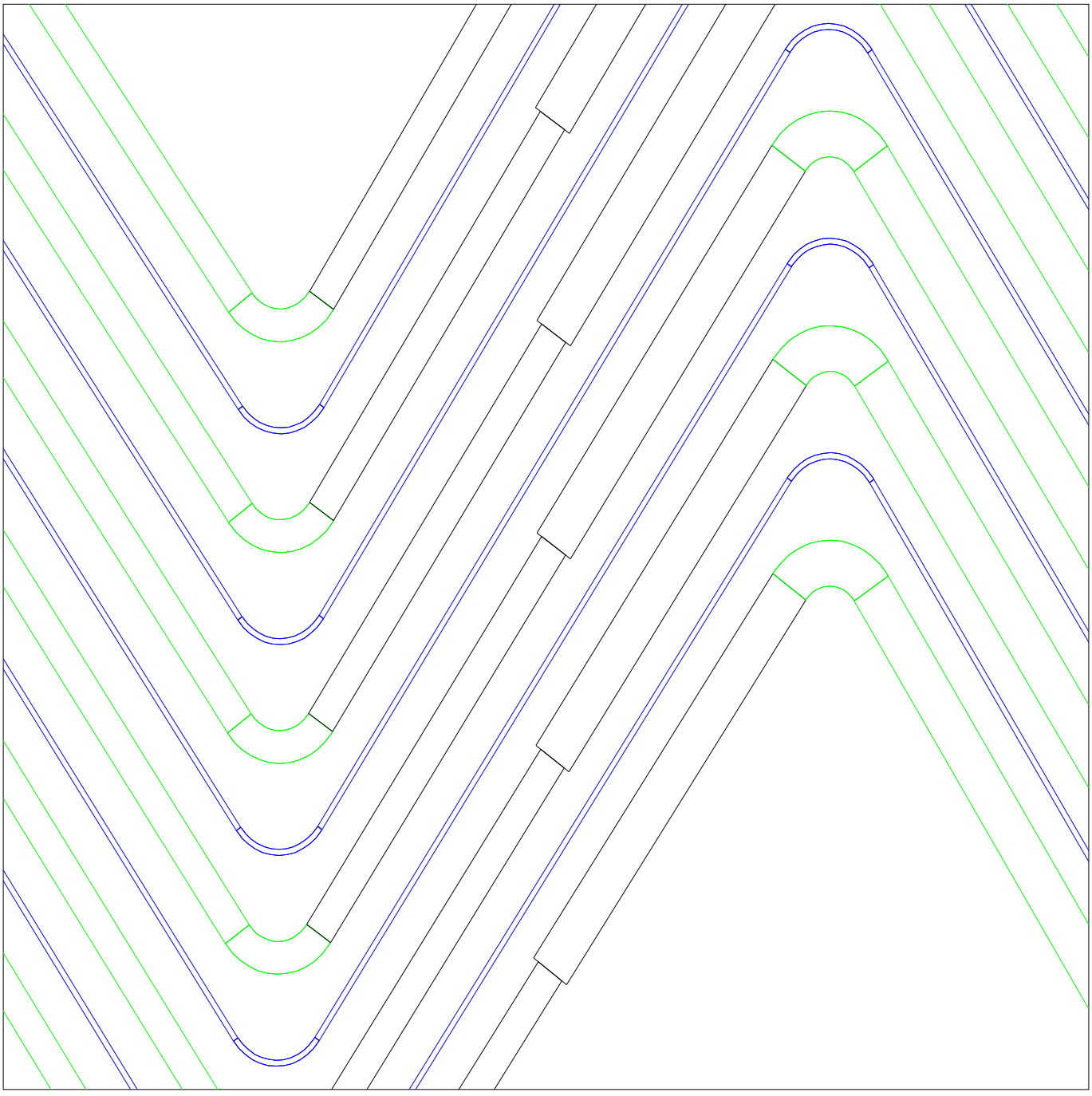

Figure 3: the new model with lead thickness increasing from 1.1 mm to 1.8 mm in the 3^{rd} sampling.

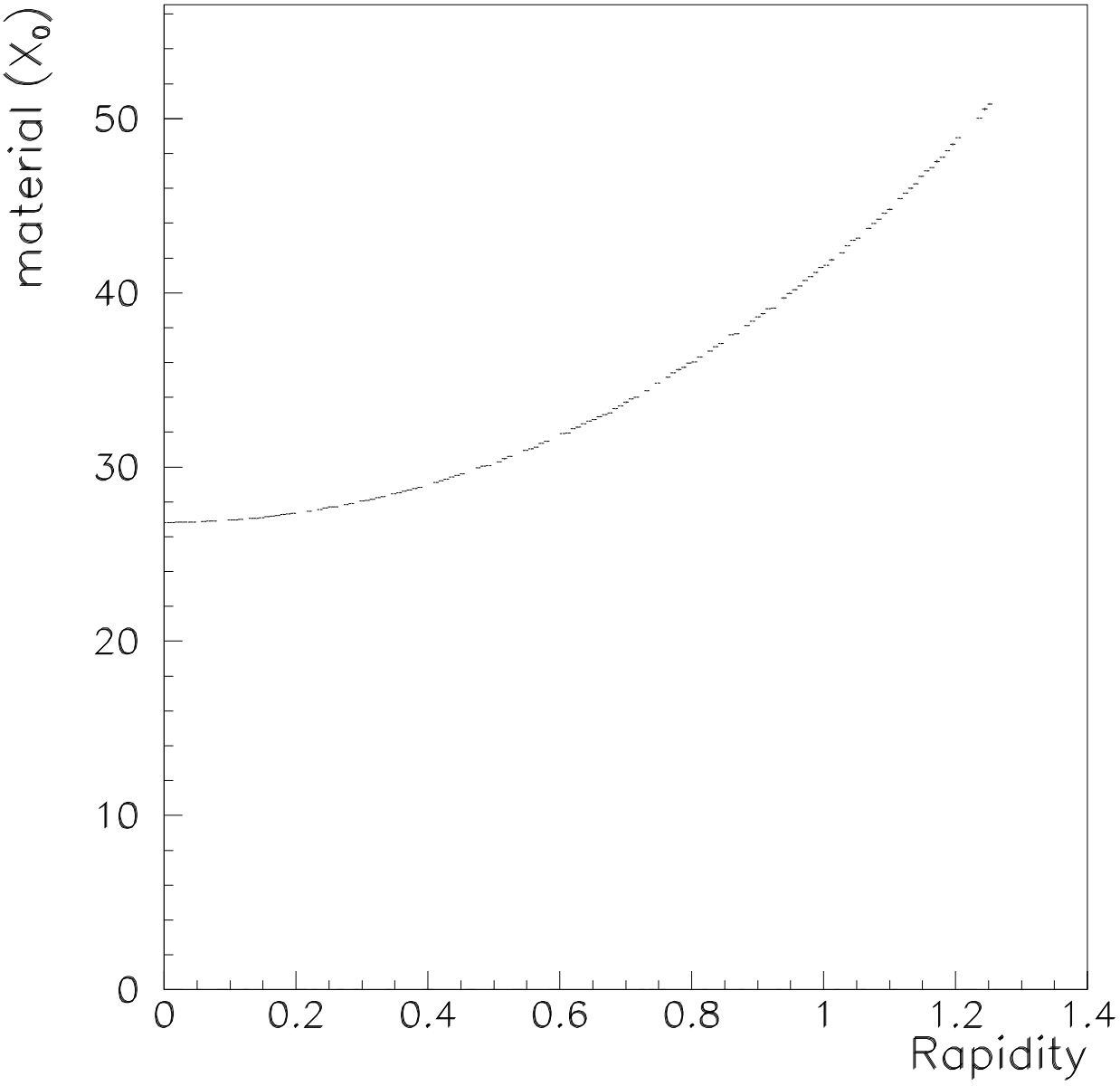

Figure 4: total radiation length after the calorimeter in the new model (number of X_0 versus η).

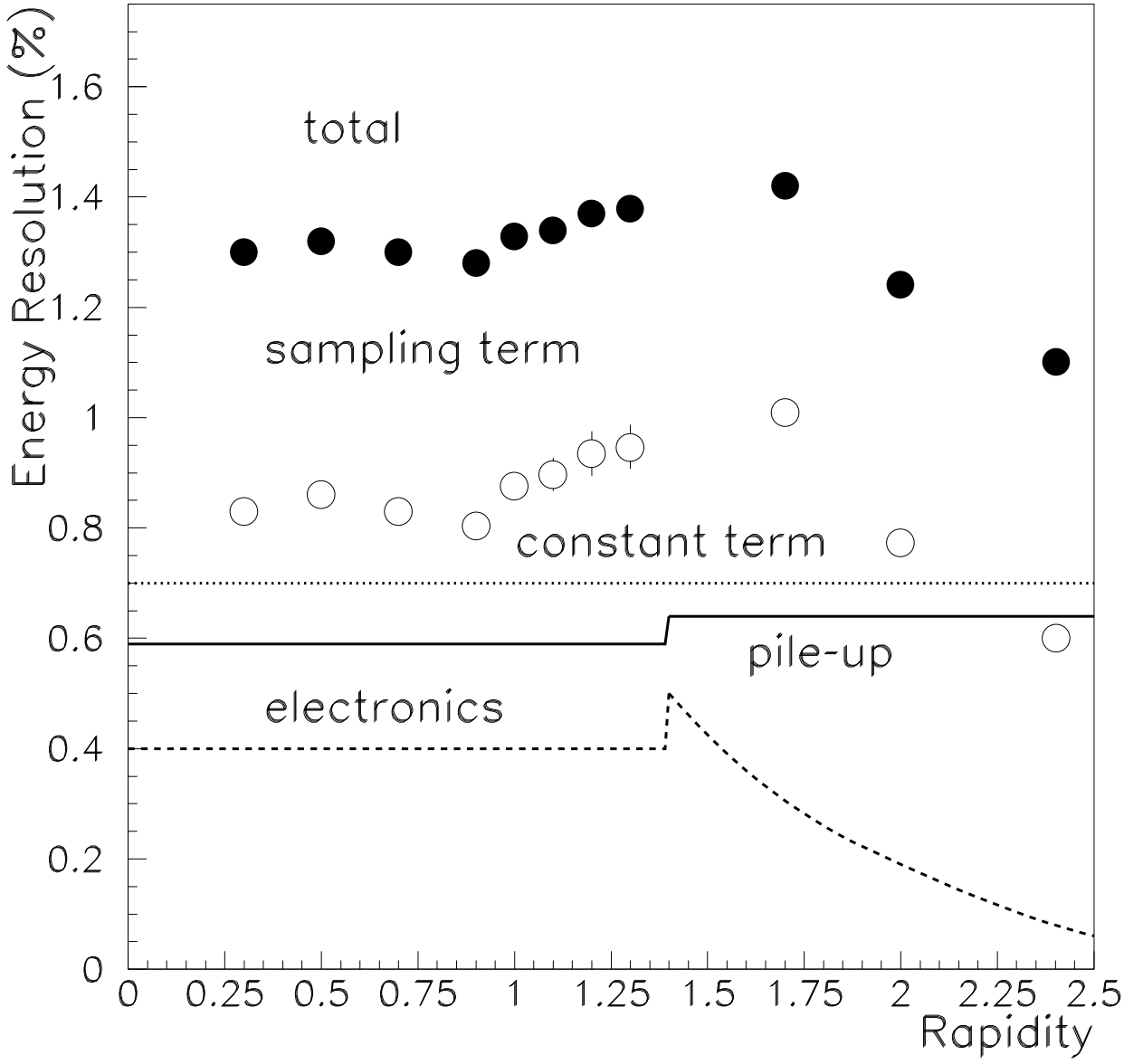

Figure 5: individual contribution to total energy resolution, with single γ's of E_T= 50 GeV in the new LKr model. 3×7 cluster sizes are used, pileup and electronics noise contributions are given for the same peaking time than in LAr with the appropriate factors.

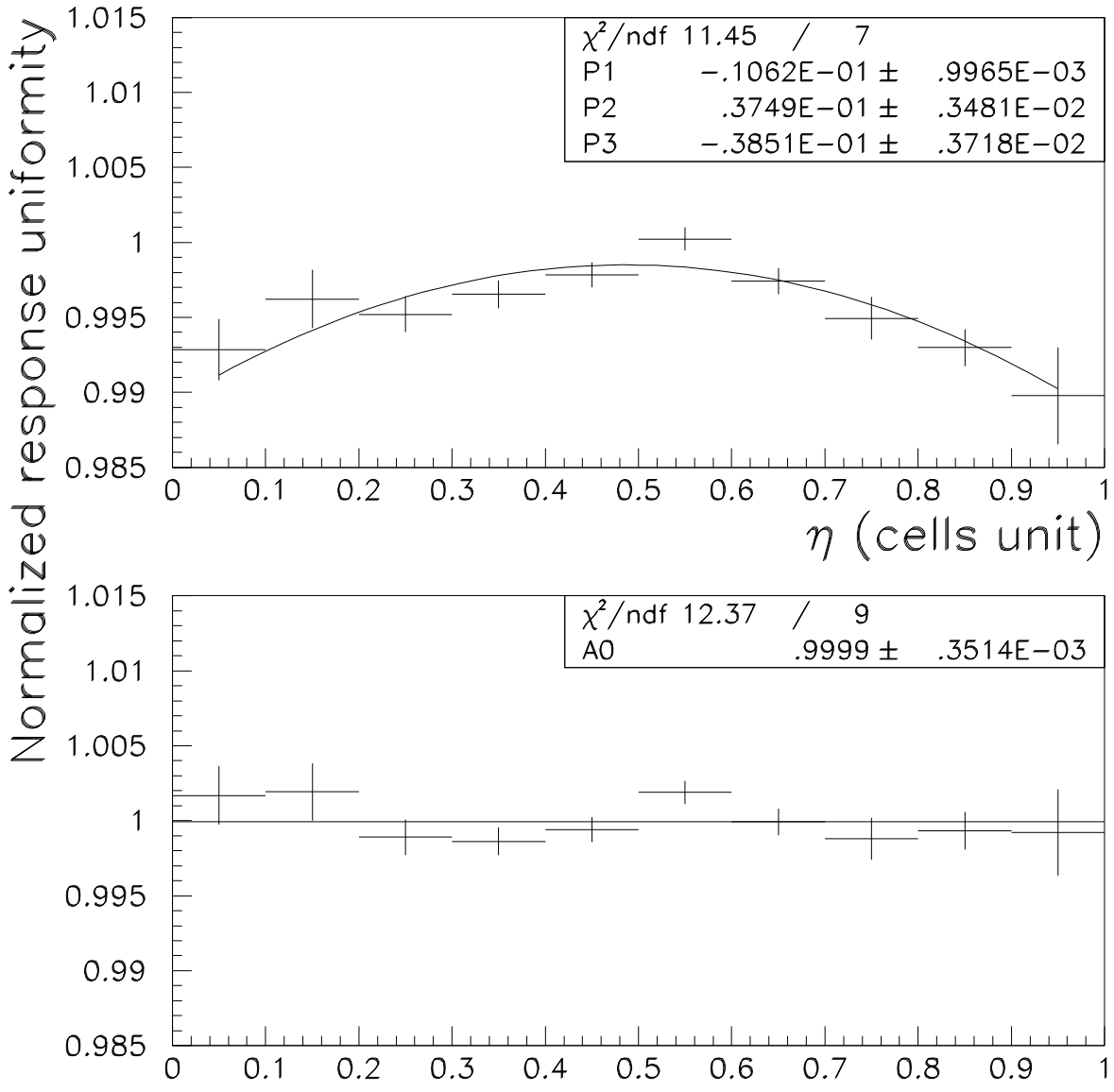

Figure 6: correction of energy response depending on the impact point in the cell in the η direction (sampling 2 granularity). Plot is obtained with single electrons of transverse energy 500 GeV at η=0.3. From top to bottom : before and after correction.

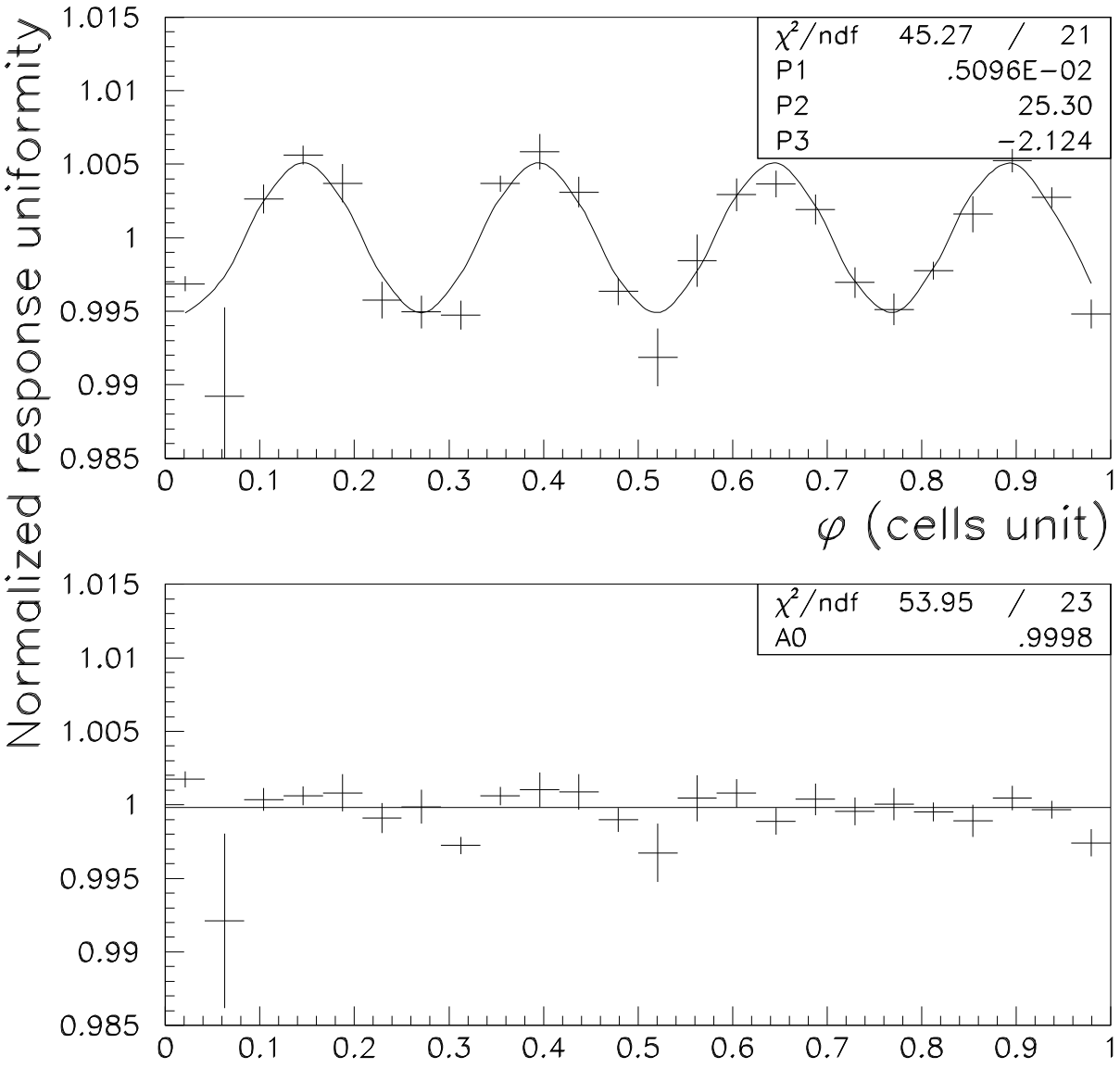

Figure 7: correction of energy response depending on the impact point in the electronics cell in the ϕ direction (sampling 2 granularity). Plot is obtained with single electrons of transverse energy 500 GeV at η=0.3. From top to bottom : before and after correction.

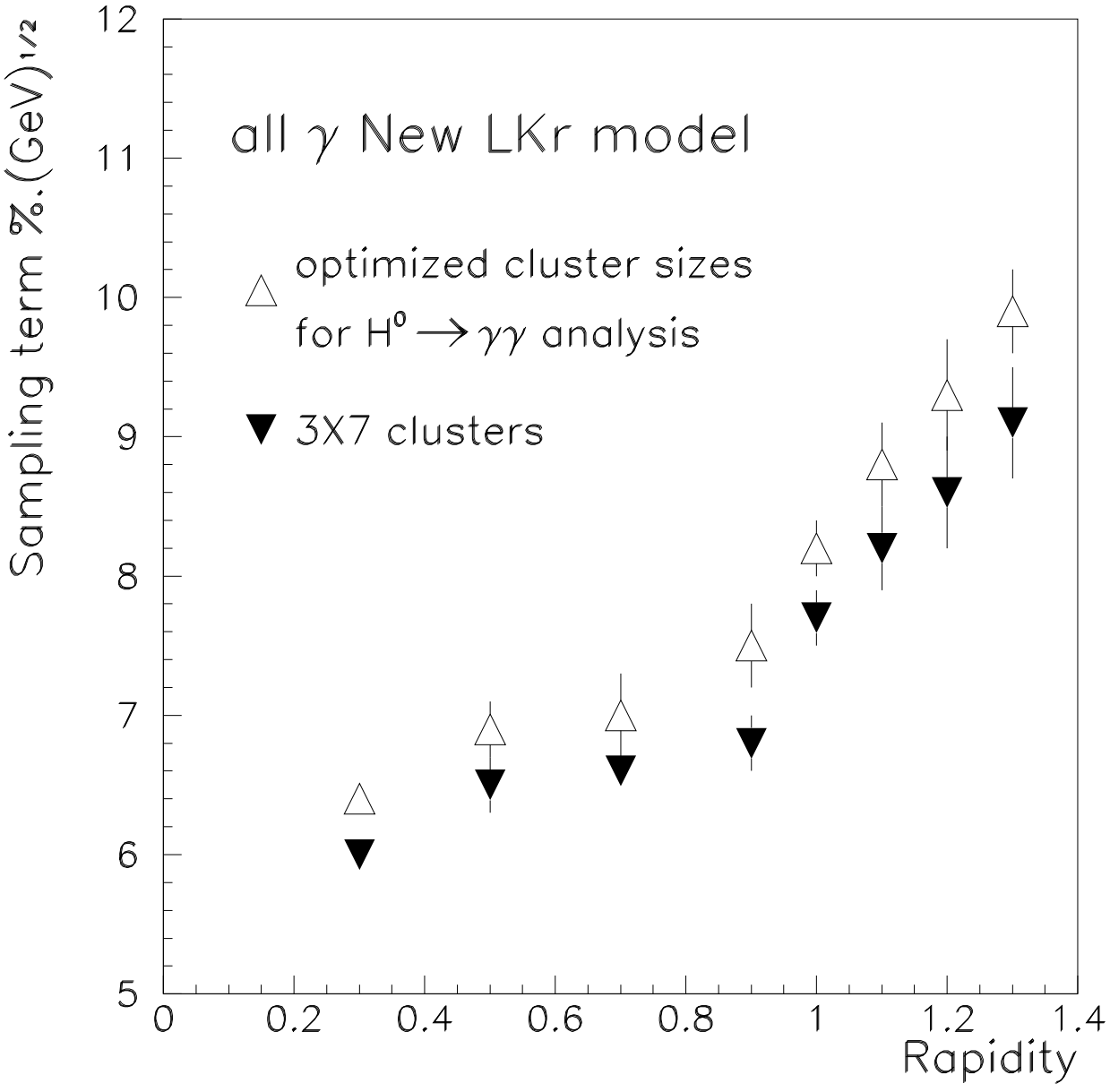

Figure 8: sampling term for single γ of transverse energy 50 GeV for the new LKr model. Energy is reconstructed with adapted cluster sizes (see table 1).

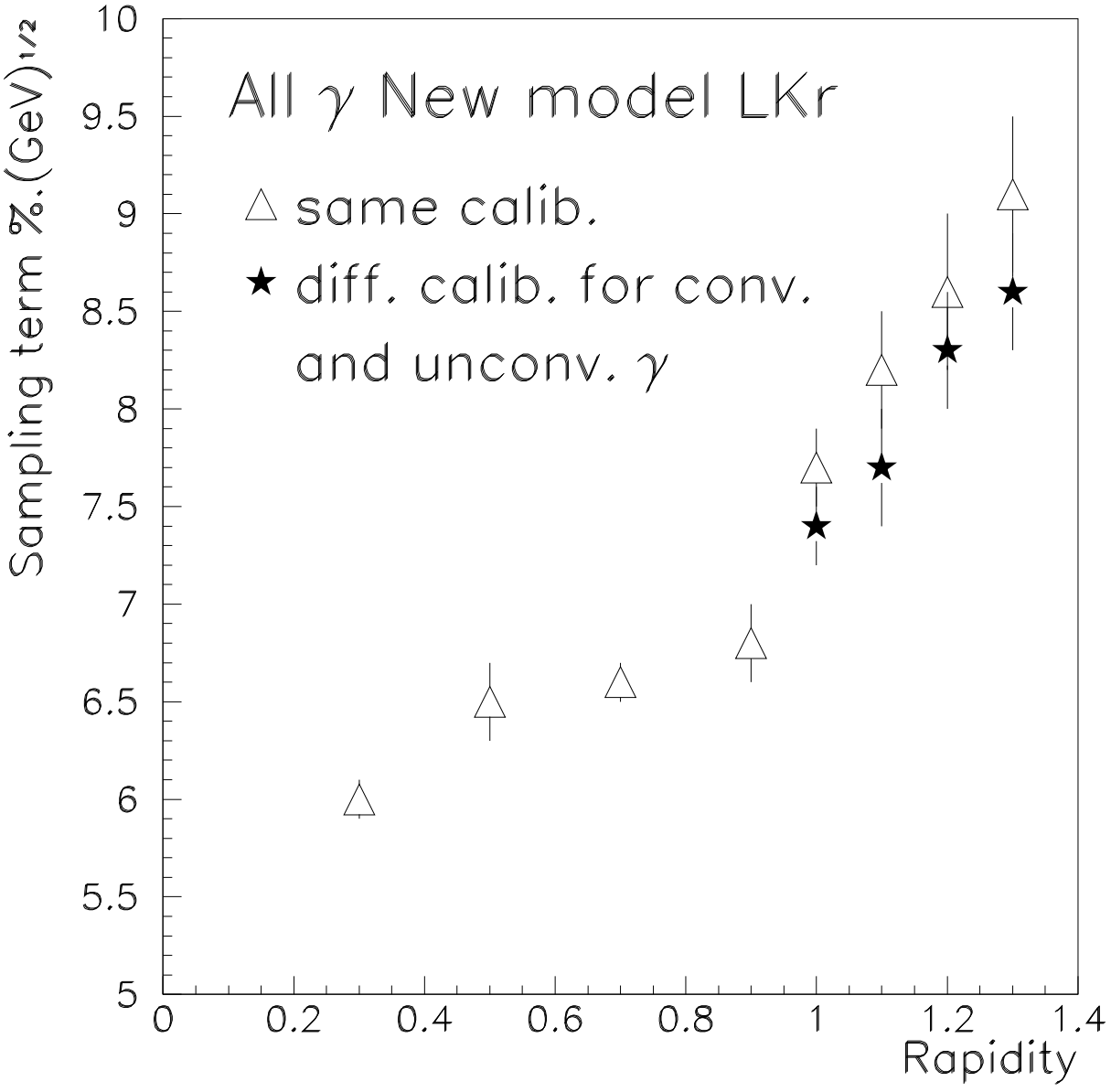

Figure 9: sampling term for single γ's of transverse energy 50 GeV for the new LKr model. Energy is reconstructed with clusters 3×7, and for rapidities higher than 1.0, two different sets of calibration are presented.

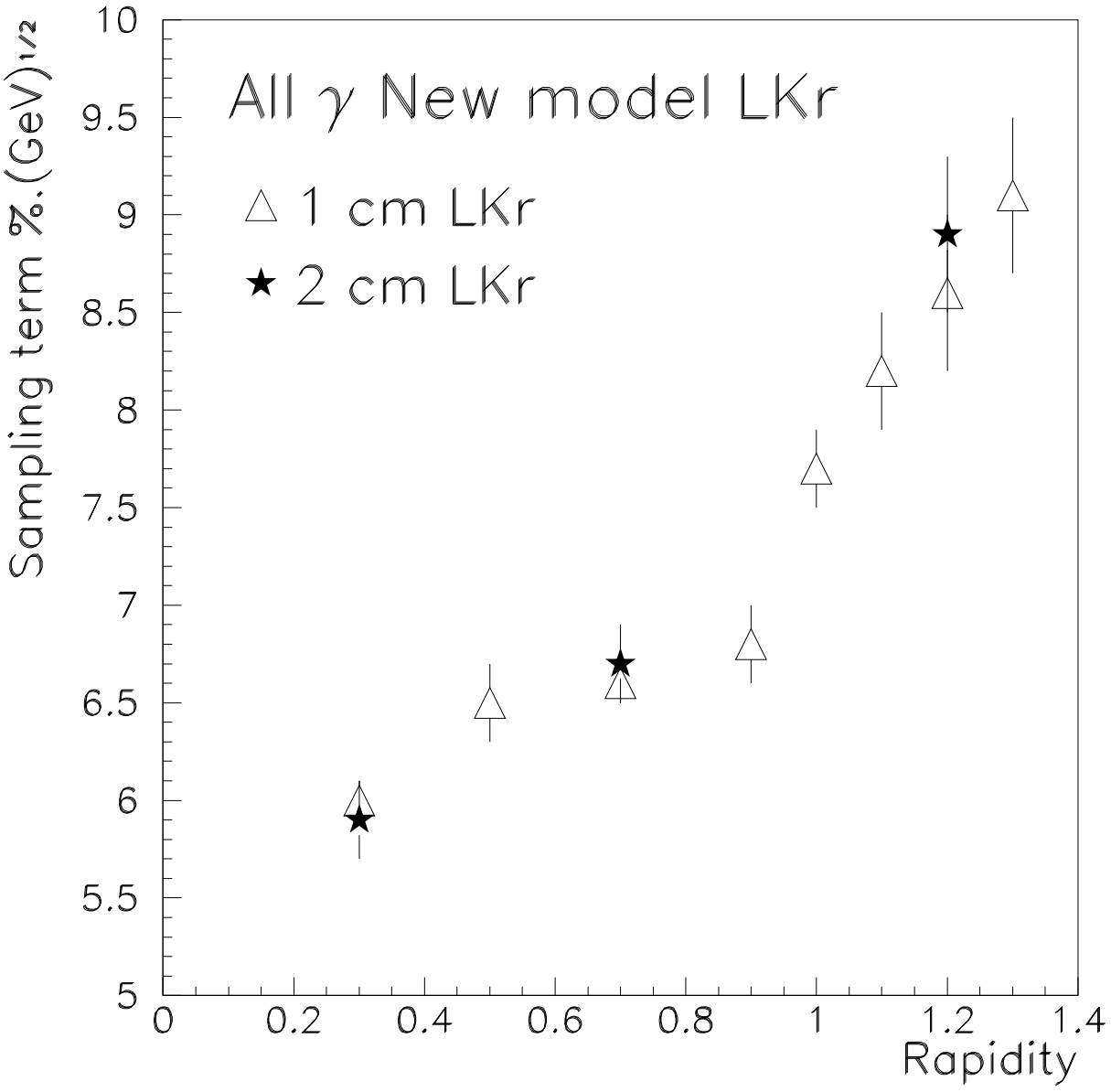

Figure 10: sampling term for single γ's of transverse energy 50 GeV for the new LKr model. Two configurations of LKr clearance in front of presampler device are presented.

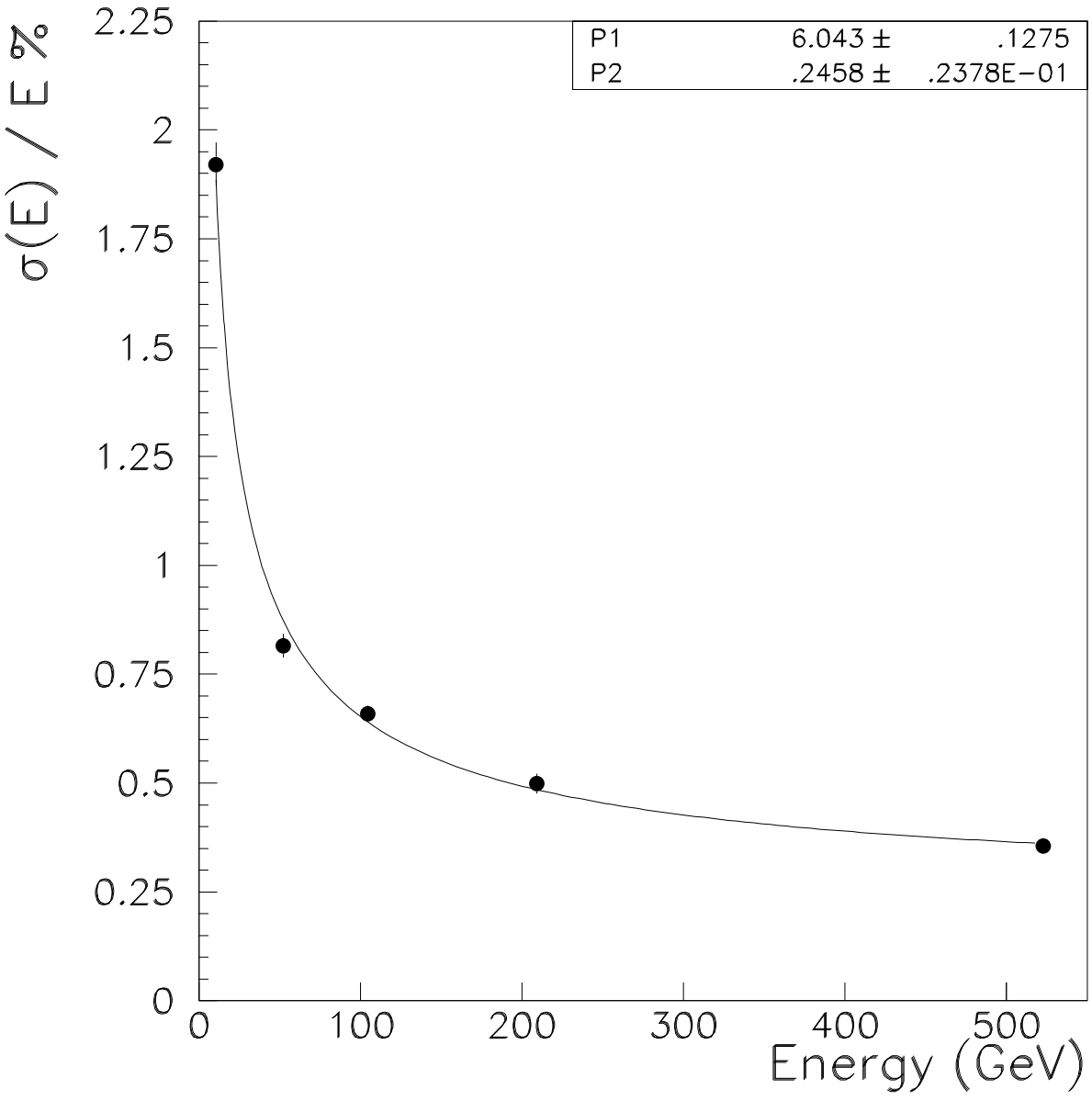

Figure 11: sampling term energy resolution with single γ's of different energy at low rapidity (η= 0.3). Parametrization is done with function : $P_1/\sqrt{E} \oplus P_2$.

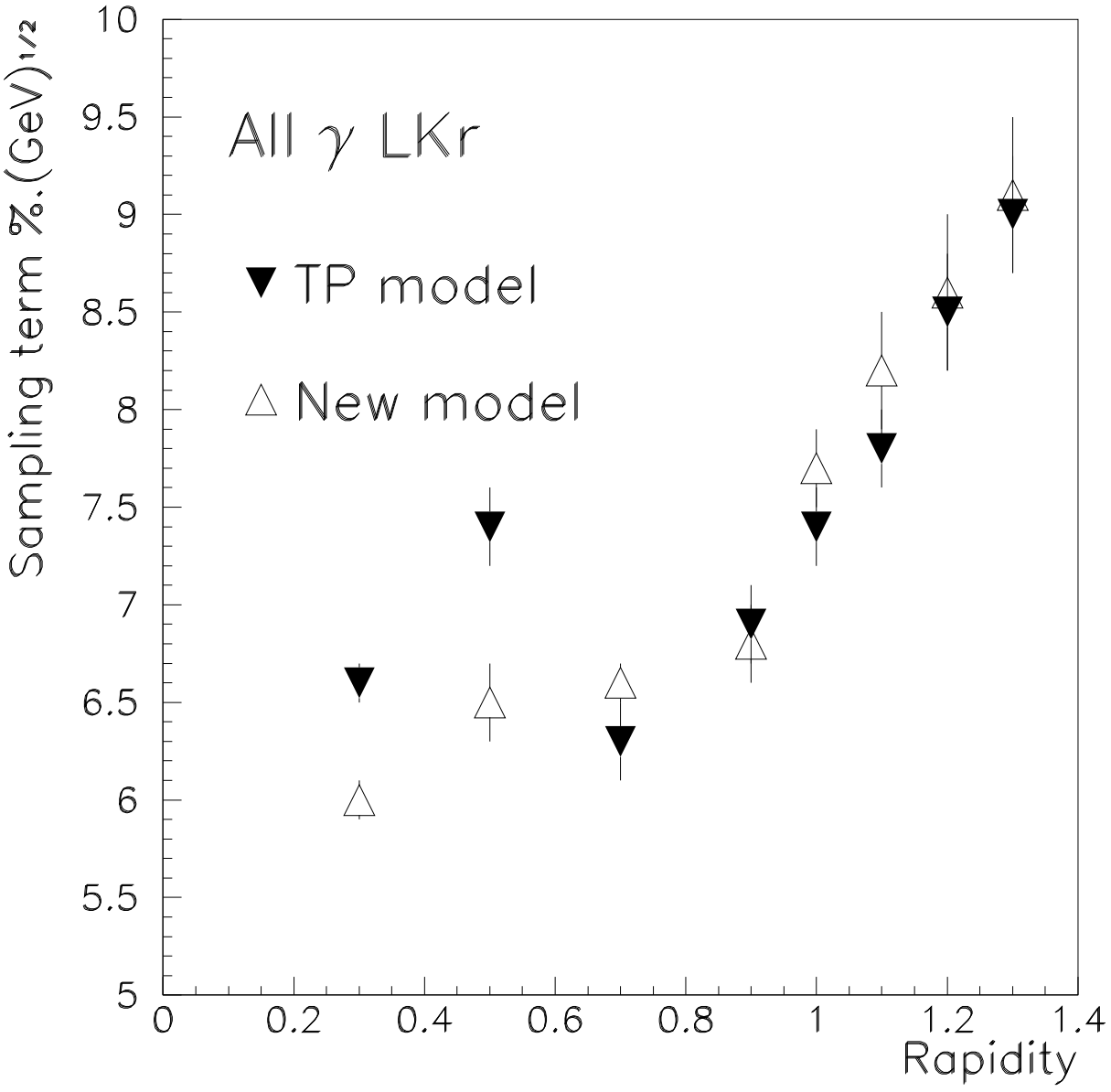

Figure 12: sampling term for single γ's of transverse energy 50 GeV for LKr TP model and for new LKr model. Energy is reconstructed with clusters 3×7 (results of TP LKr model have been revisited).

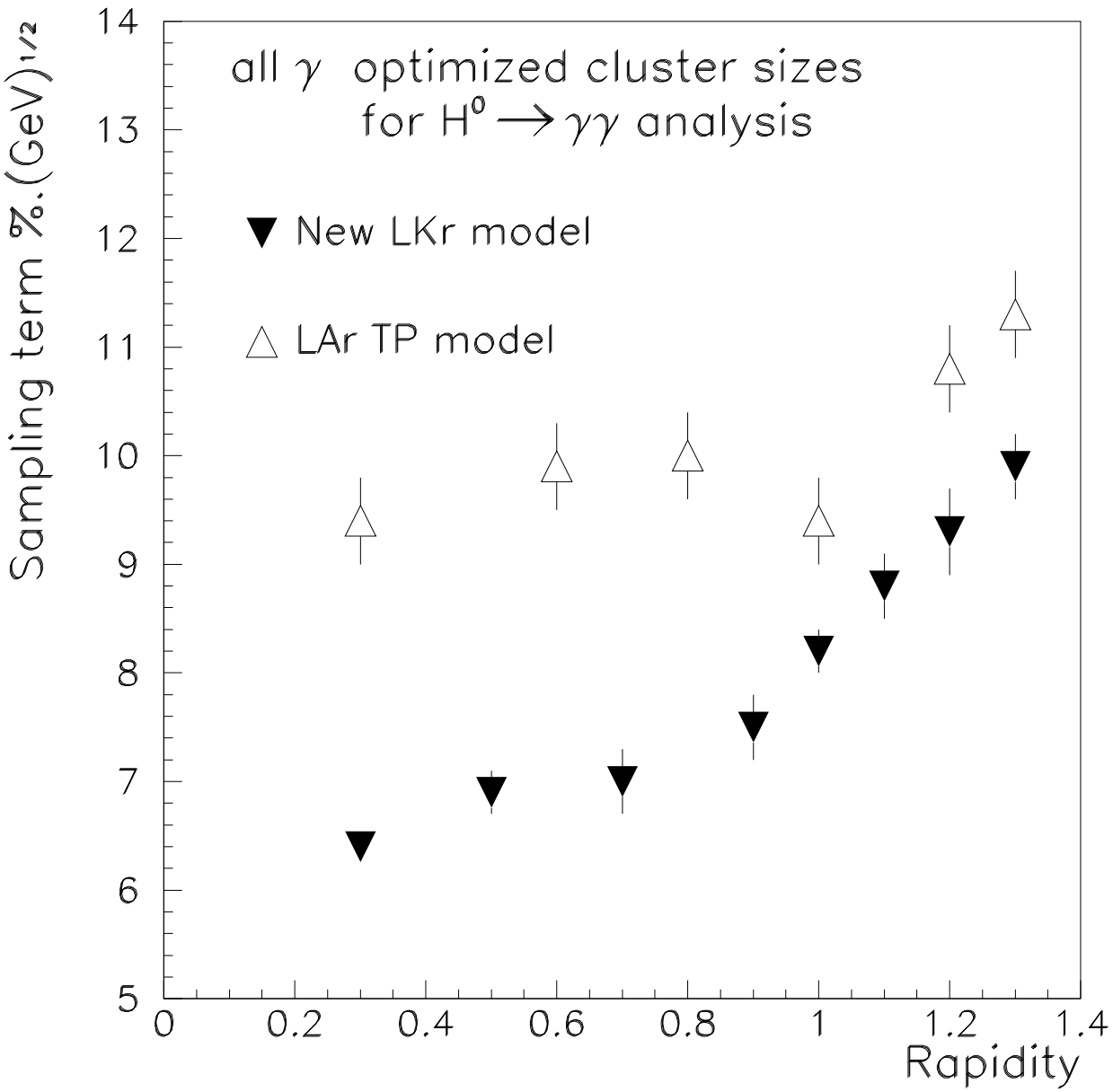

Figure 13: comparison of sampling term in LAr TP model case and for the new LKr model. Single γ's of E_T=50 GeV are used and energy reconstruction is done with clusters adapted to converted and to unconverted γ's (in case of LAr, 24 strips in the η direction for sampling S_1 of barrel part are used even in case of unconverted γ's).

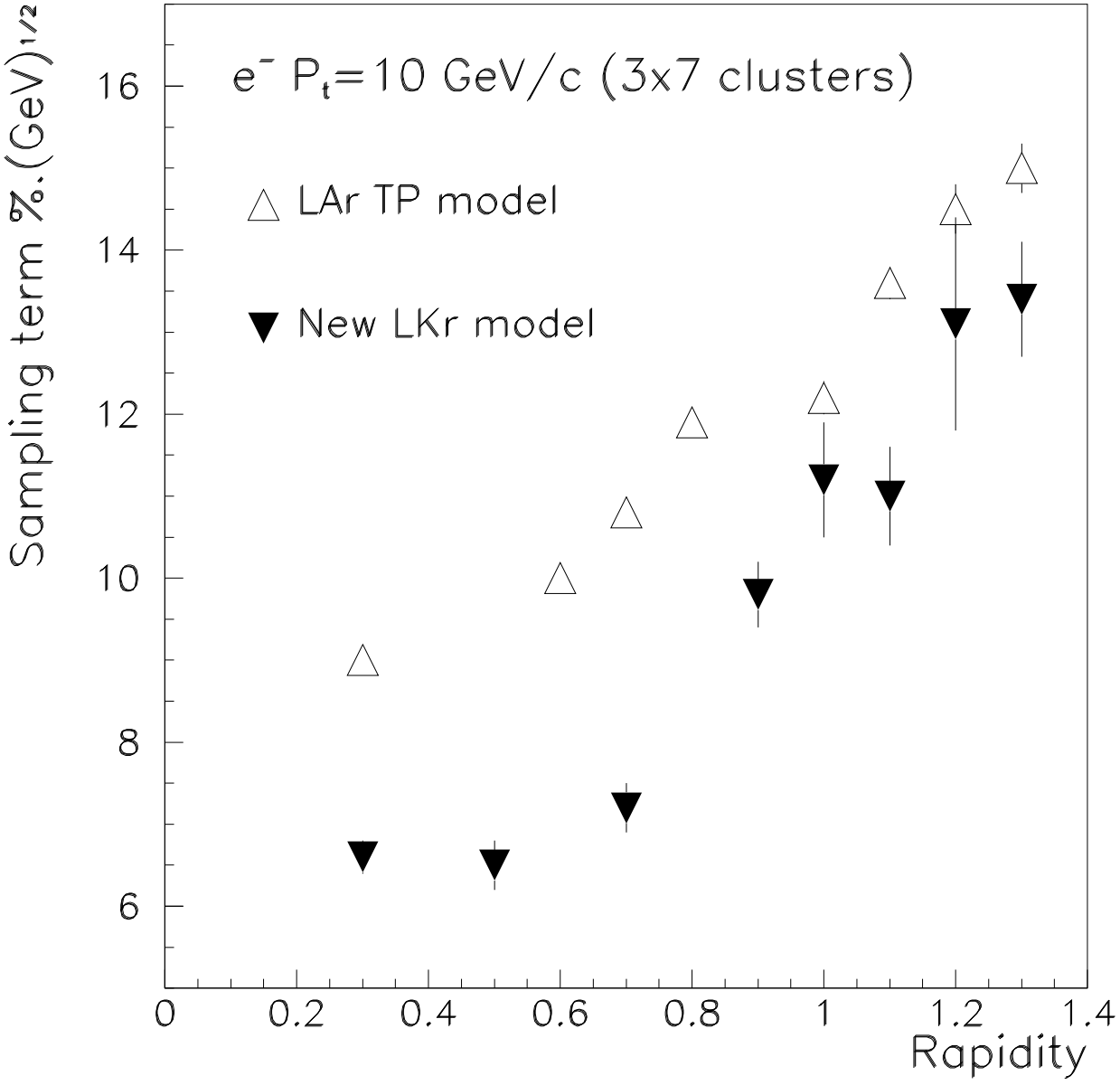

Figure 14: sampling term for single electrons of transverse energy 10 GeV for the new LKr model. Energy is reconstructed with clusters 3×7, and calibration used was obtained with γ's of transverse energy 50 GeV.

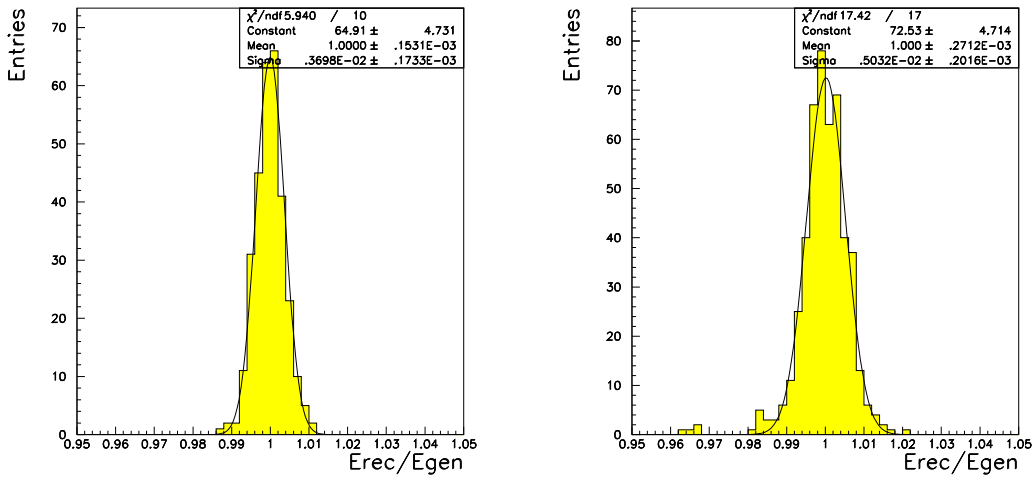

Figure 15: energy reconstruction for electrons of E_T= 500 GeV at η= 0.3 (modulation corrections have been applied). Left : the new LKr geometry filled with LKr, right : the new LKr geometry filled with LAr (in that case deposited energy in 1^{rst} compartment of HADCAL has been added when it's possible).

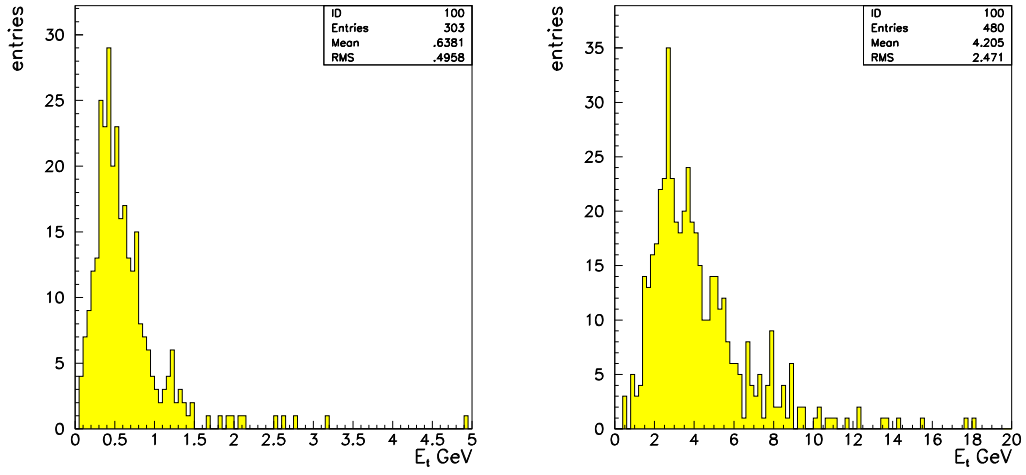

Figure 16: transverse energy leakage in HADCAL 1^{rst} compartment. Left : the new LKr geometry filled with LKr, right : the new LKr geometry filled with LAr (in that case entries above 1 GeV are used).

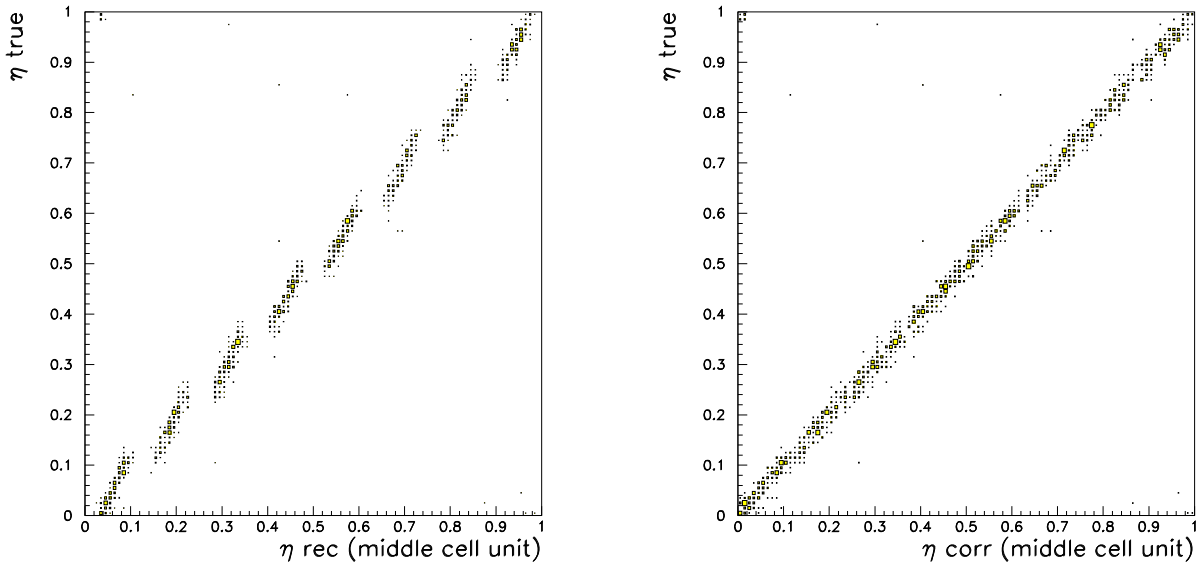

Figure 17: correction of "S-shape" profile in sampling 1. Left : before, right : after.

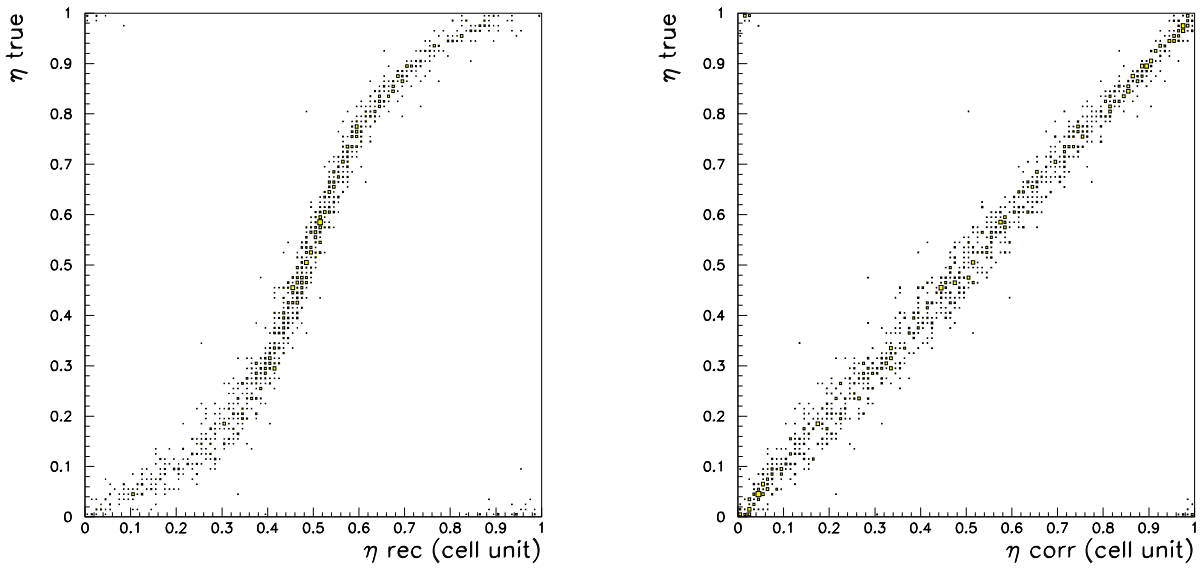

Figure 18: correction of "S-shape" profile in sampling 2+3. Left : before, right : after.

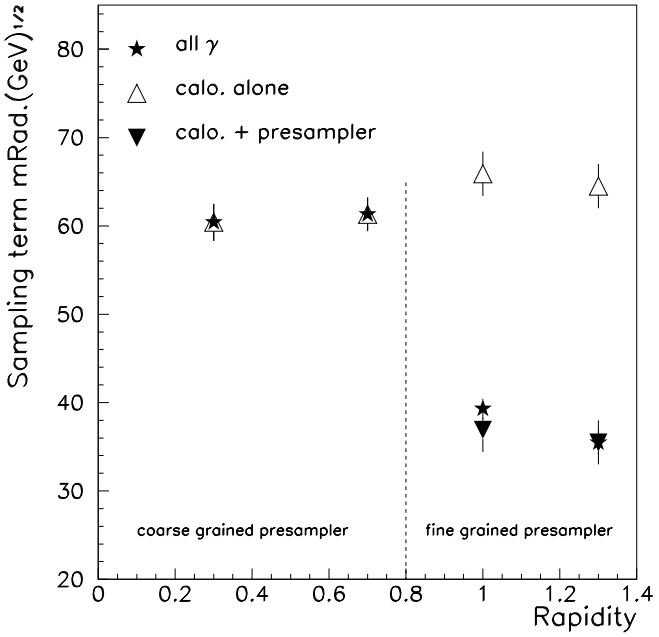

Figure 19: angular resolution for pointing of z-vertex obtained with single γ's of transverse energy 50 GeV (stars present the expected resolution for γ's of Higgs signal).

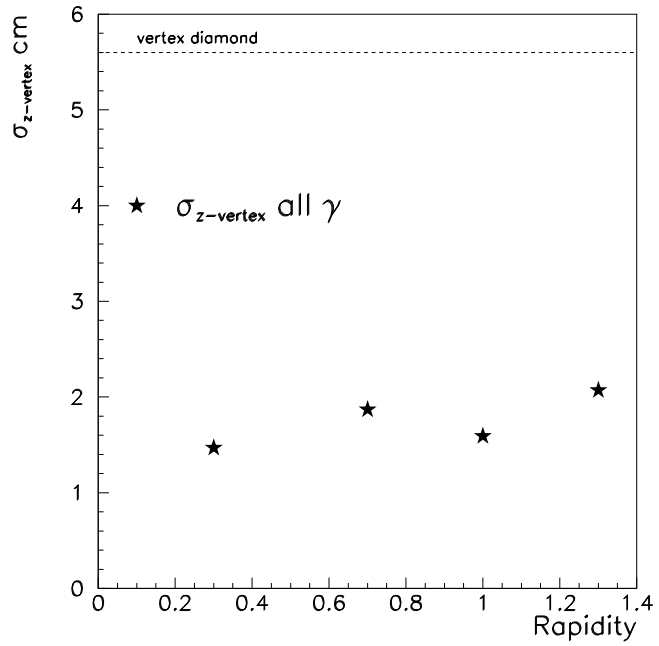

Figure 20: resolution on z-vertex position obtained with pointing.

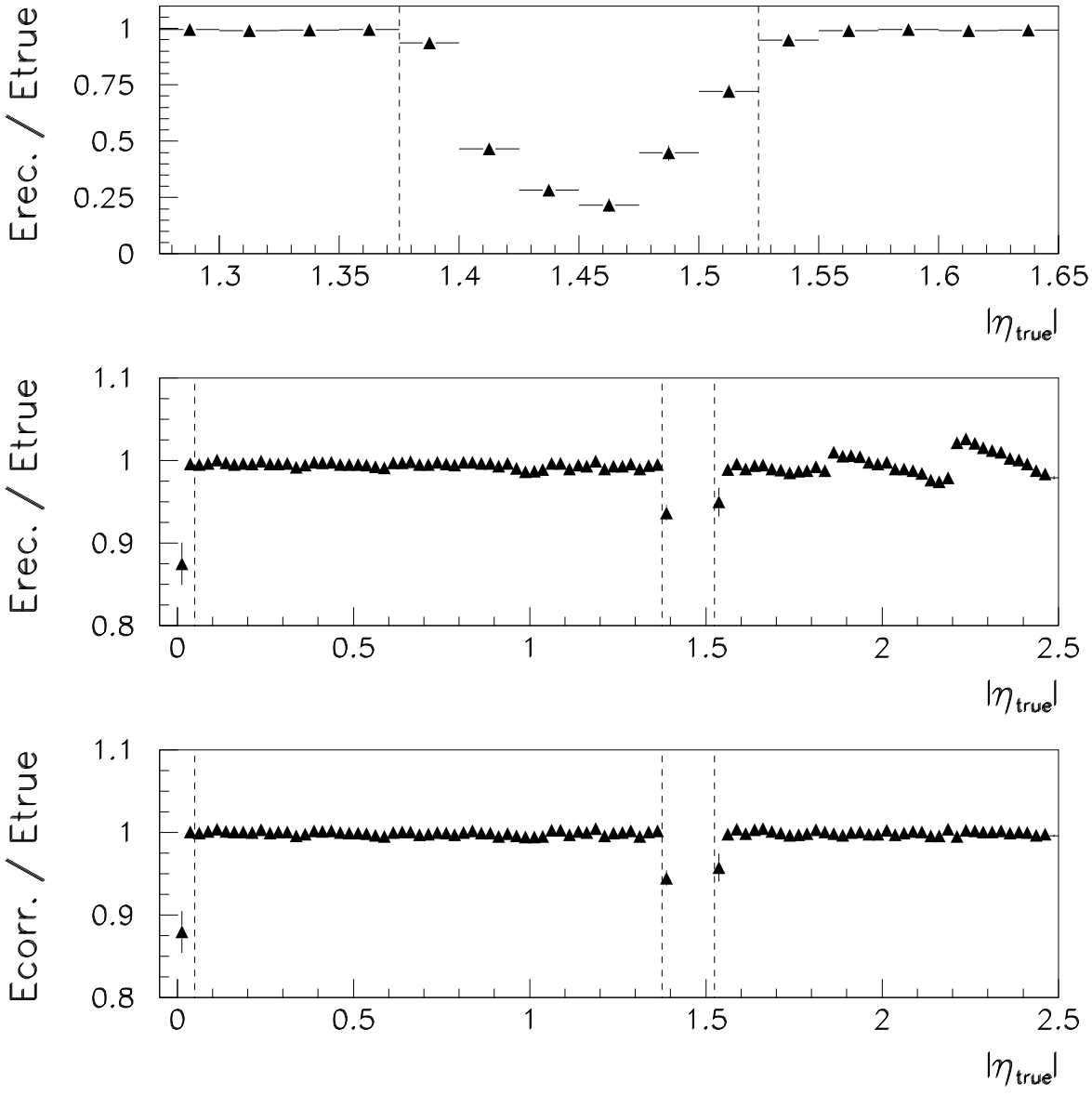

Figure 21: ratio of reconstructed energy to incident energy versus rapidity. From top to bottom : zoom of transition region between barrel and endcap calorimeter, ratio before corrections, ratio after correction.

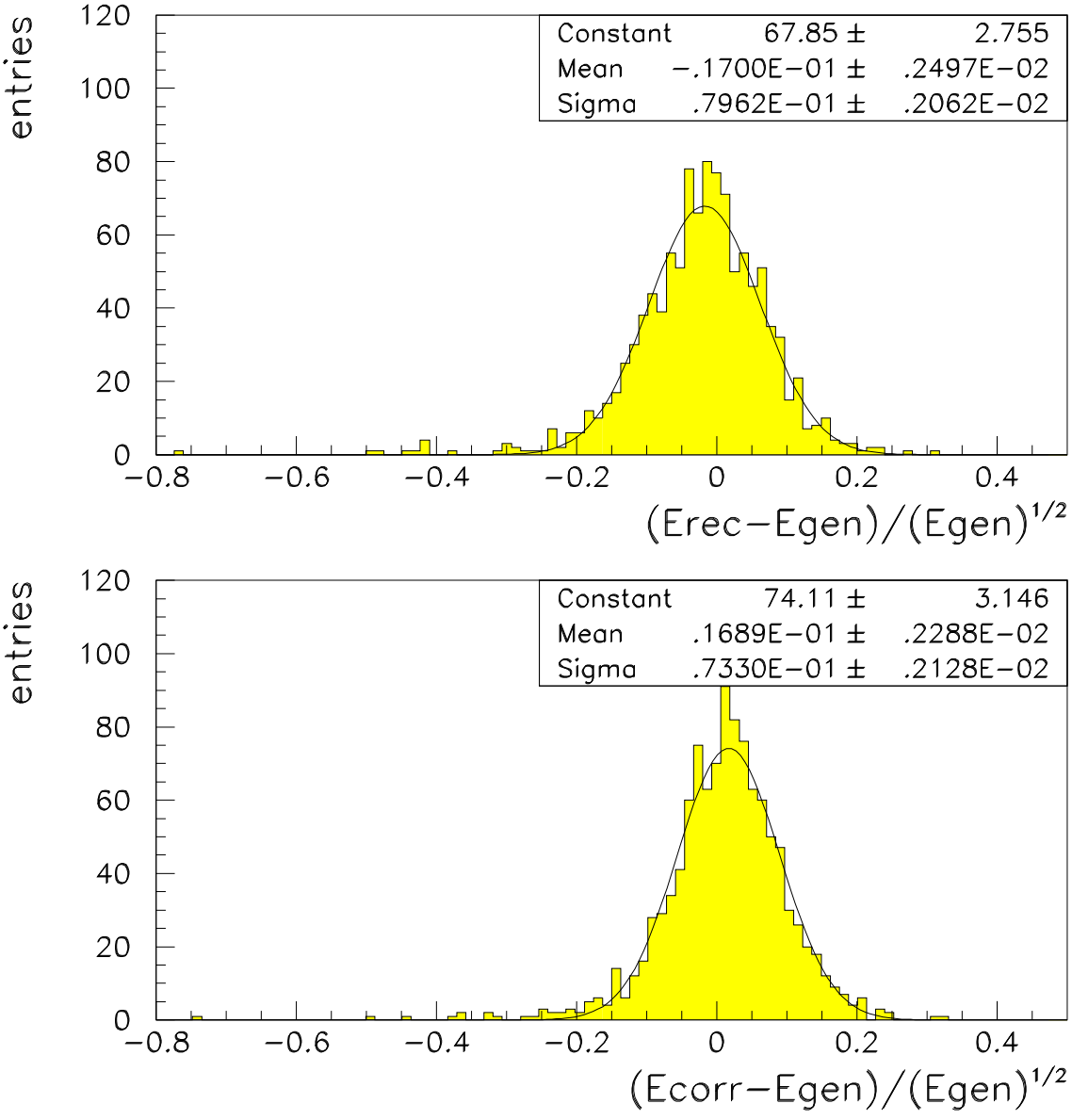

Figure 22: sampling term of γ's from H^o signal before and after modulation corrections, for γ's in the barrel (sigma of the distribution is the sampling term value).

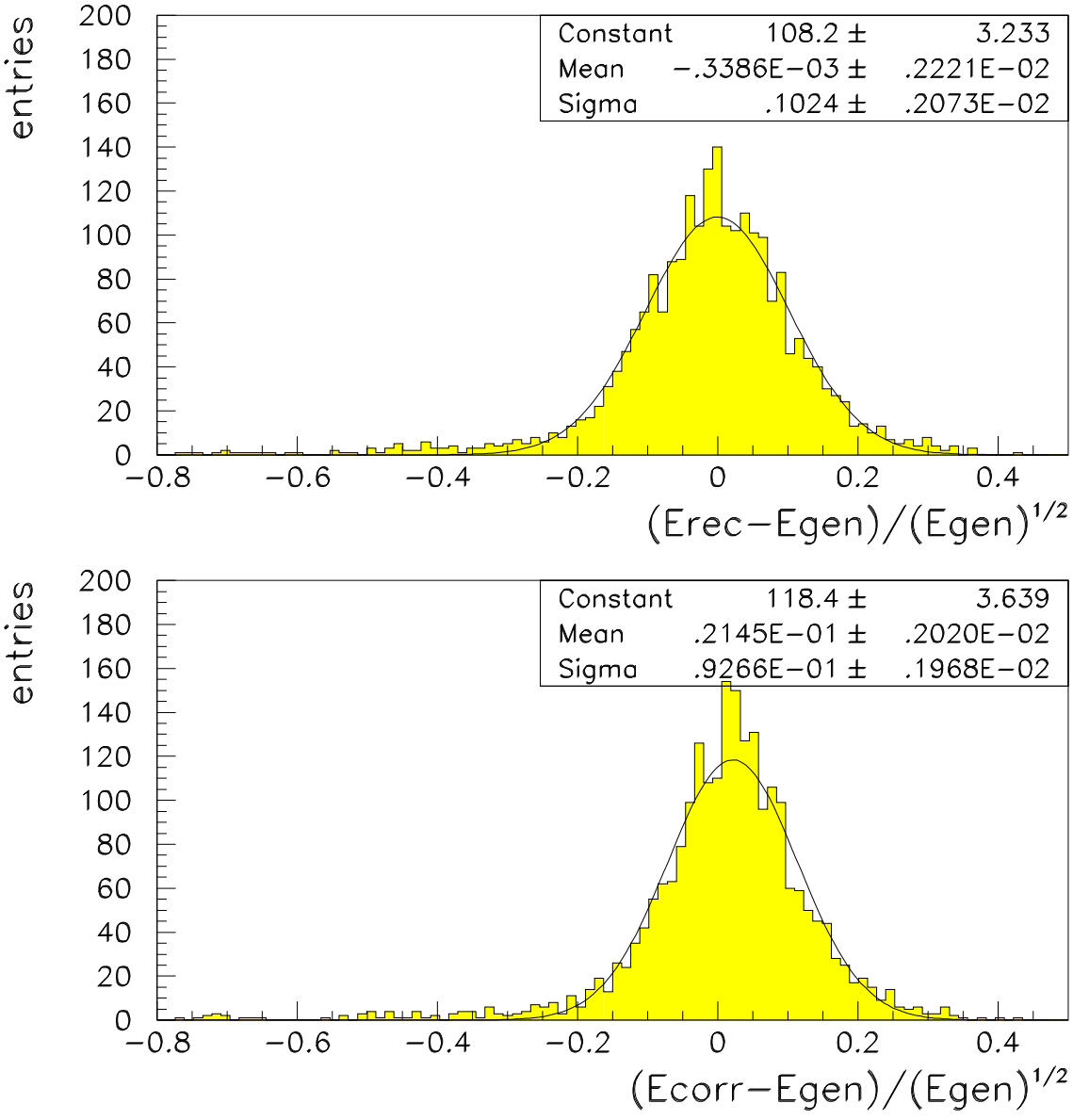

Figure 23: sampling term of γ's from H^o signal before and after modulation corrections, for γ's over all the considerered η coverage (sigma of the distribution is the sampling term value).

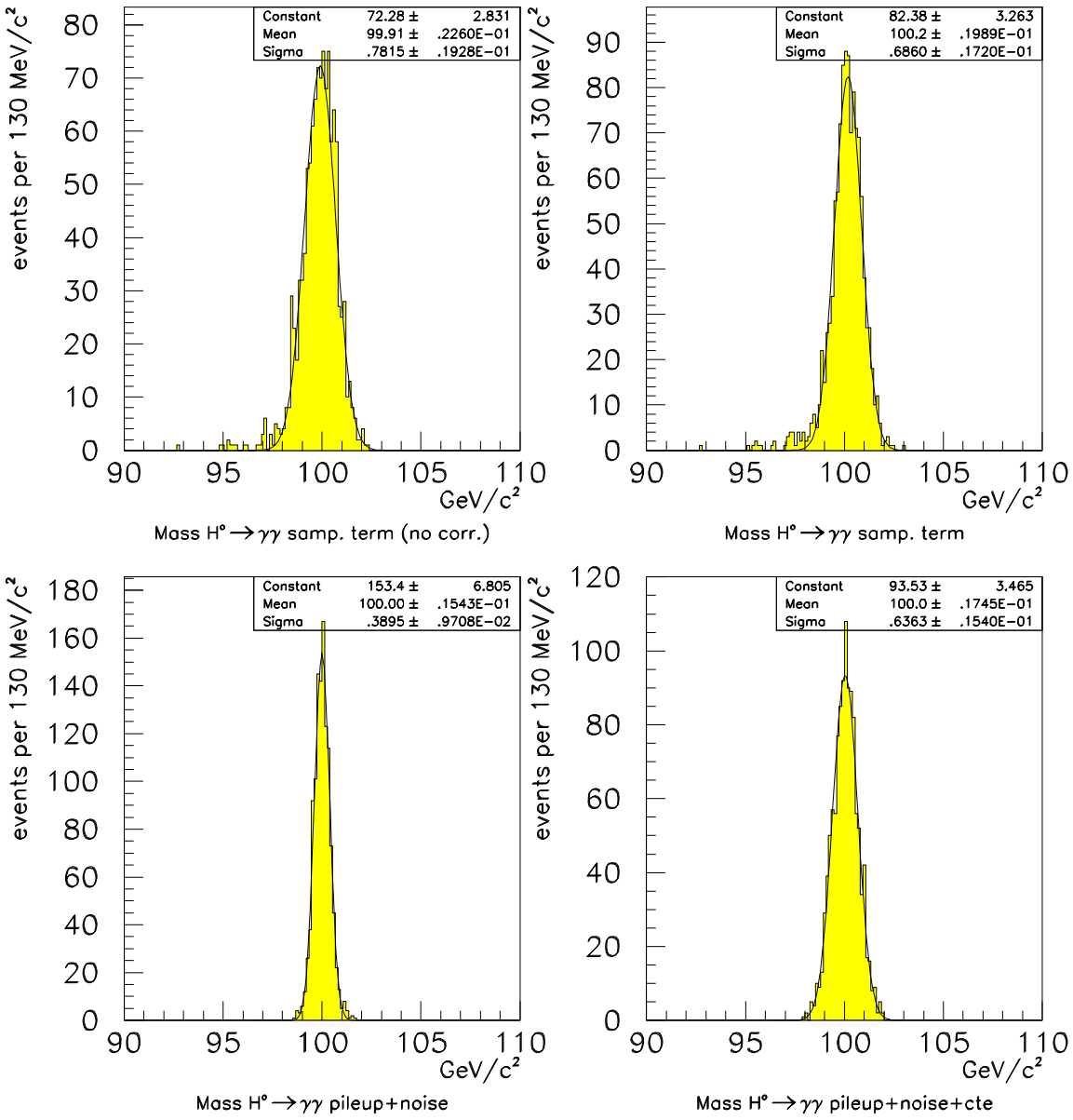

Figure 24: individual contributions to mass resolution. from top to bottom, and from left to right : sampling term before and after modulation corrections, then pileup + electronics noise contribution and finally pileup + electronics noise + constant term contribution.

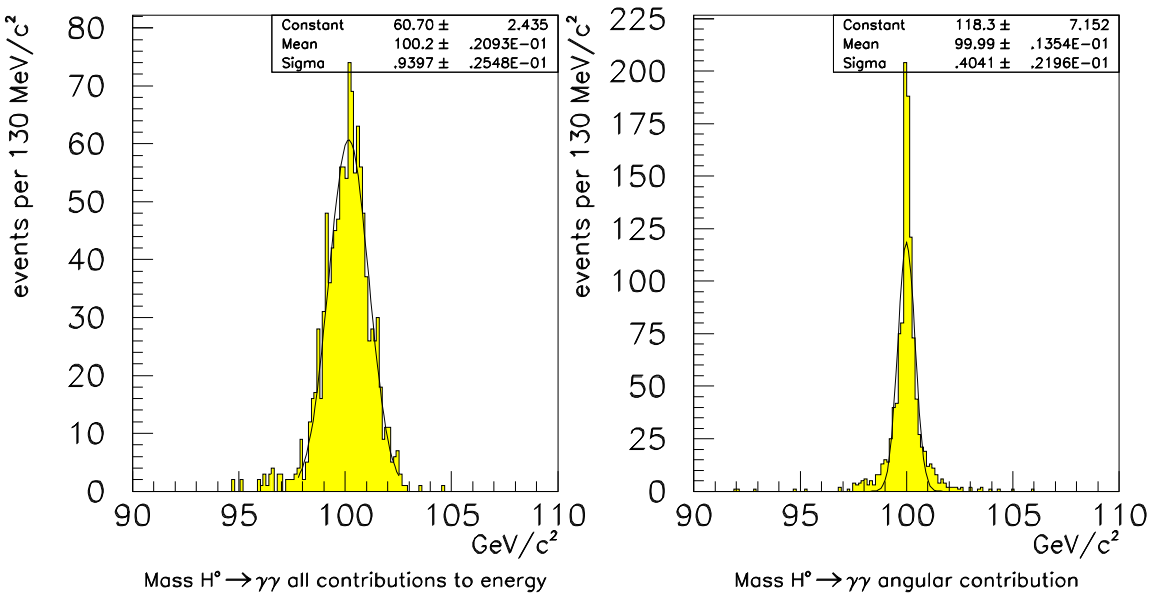

Figure 25: individual contributions to mass resolution. From left to right : total energy contribution and angular contribution.

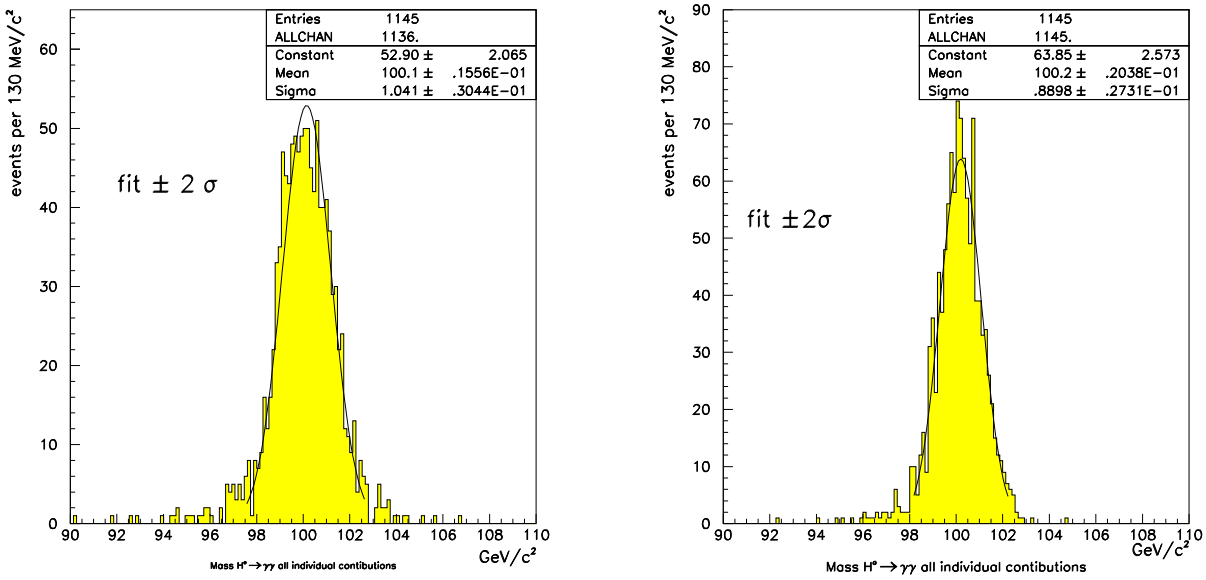

Figure 26: $\sigma_{m_{H^o}}$ for all γ's fitted at ± 2 σ from mean value. Left : for high luminosity, right : for low luminosity.

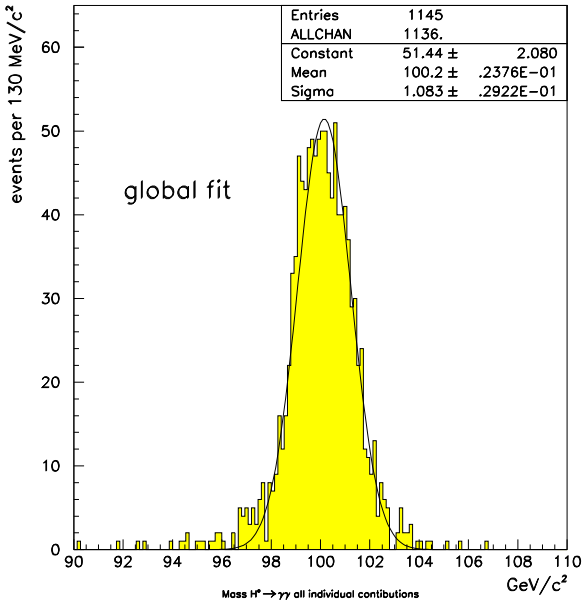

Figure 27: $\sigma_{m_{H^o}}$ for all γ's. Global fit is performed.

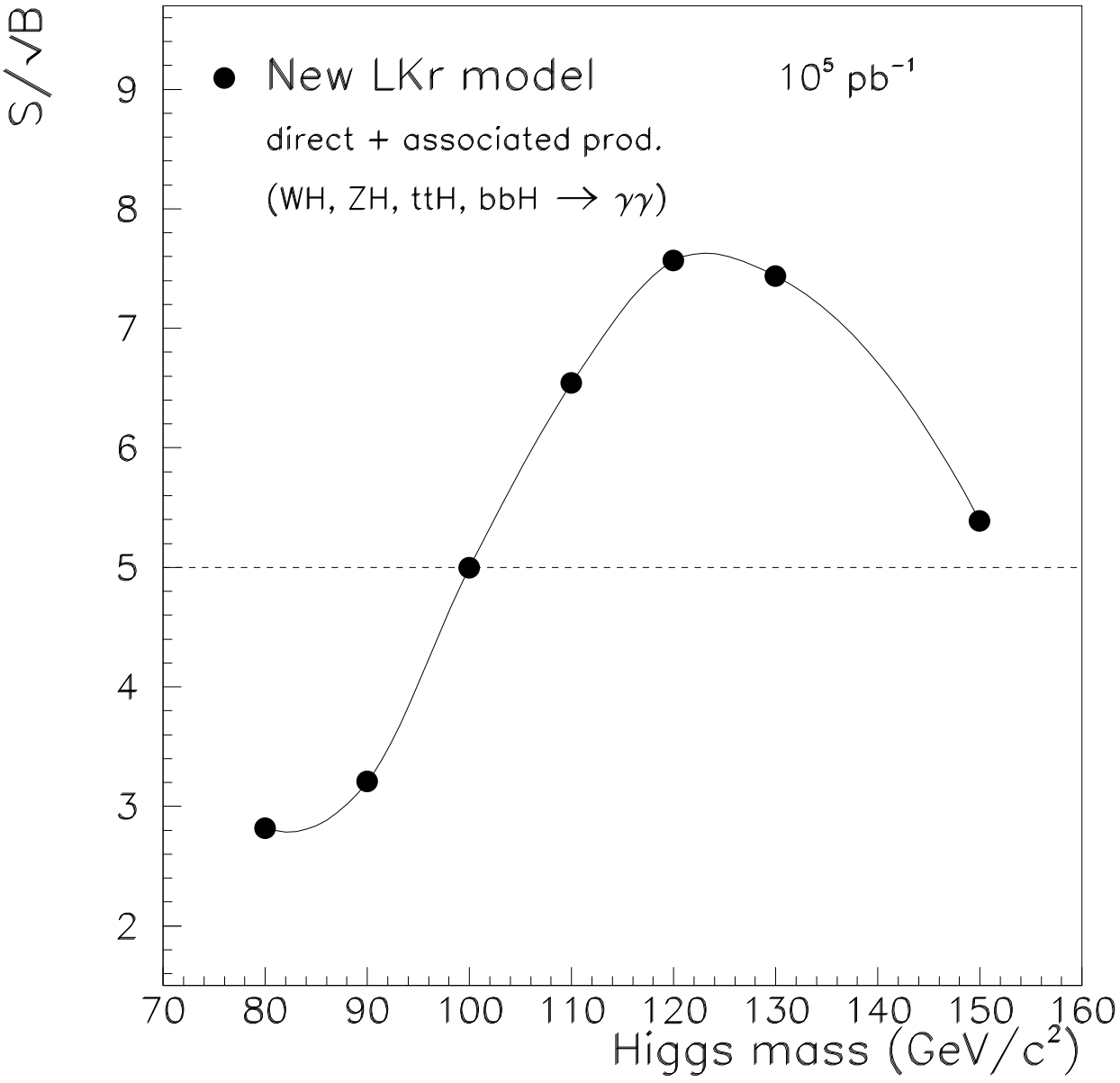

Figure 28: expected $S/\sqrt{B}$ for $H^o \rightarrow \gamma\gamma$ signal in ATLAS with LKr option. Values are presented for an integrated luminosity of 10^5 pb^{-1}.

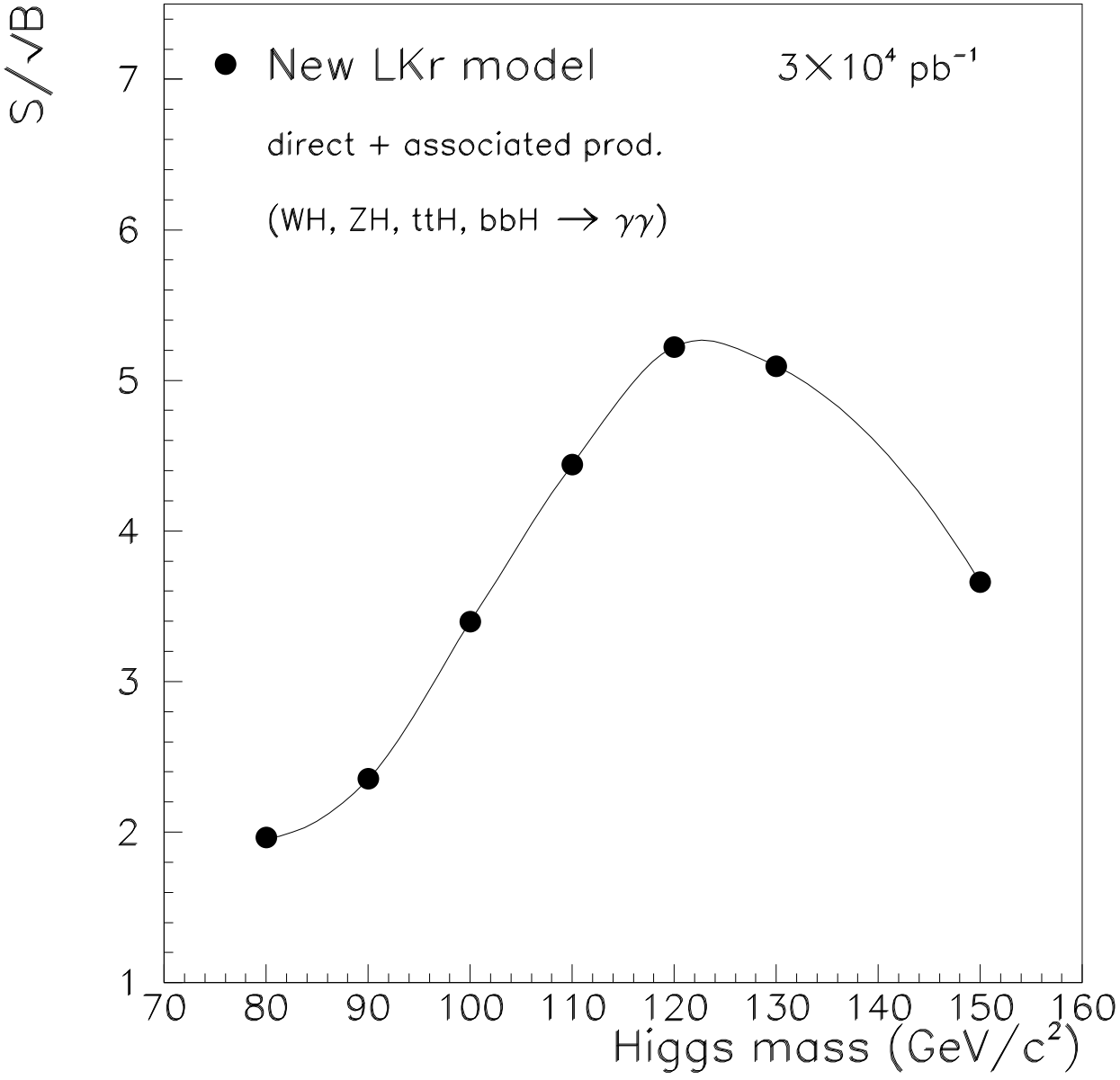

Figure 29: expected $S/\sqrt{B}$ for $H^o \rightarrow \gamma\gamma$ signal in ATLAS with LKr option. Values are presented for an integrated luminosity of 3.10^4 pb^{-1}.

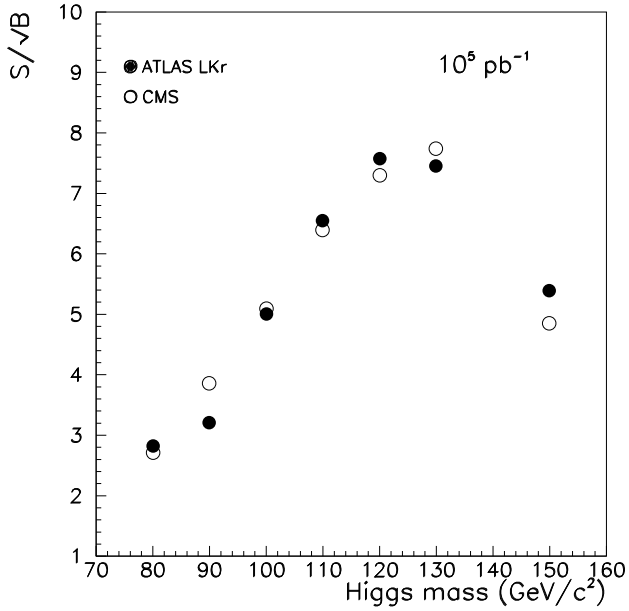

Figure 30: comparison of expected $S/\sqrt{B}$ for $H^o \rightarrow \gamma\gamma$ signal in ATLAS with LKr and in CMS (same analysis for points which are detector independant). Values are presented for an integrated luminosity of 10^5 pb^{-1}.

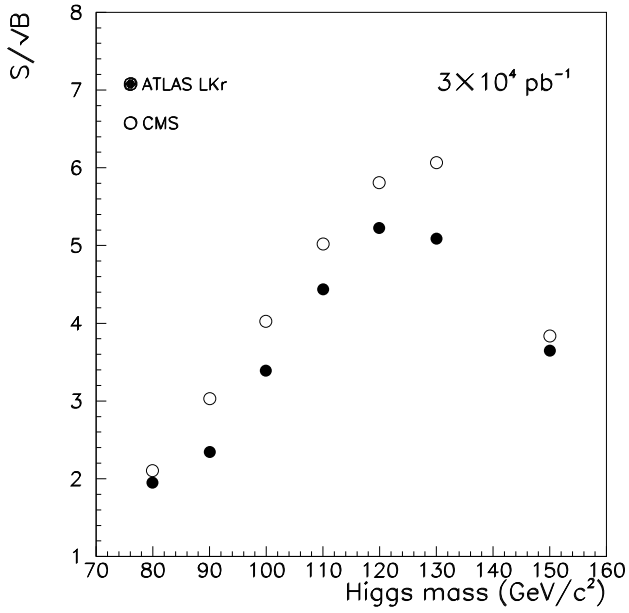

Figure 31: comparison of expected $S/\sqrt{B}$ for $H^o \rightarrow \gamma\gamma$ signal in ATLAS with LKr and in CMS (same analysis for points which are detector independant). Values are presented for an integrated luminosity of 3.10^4 pb^{-1}.

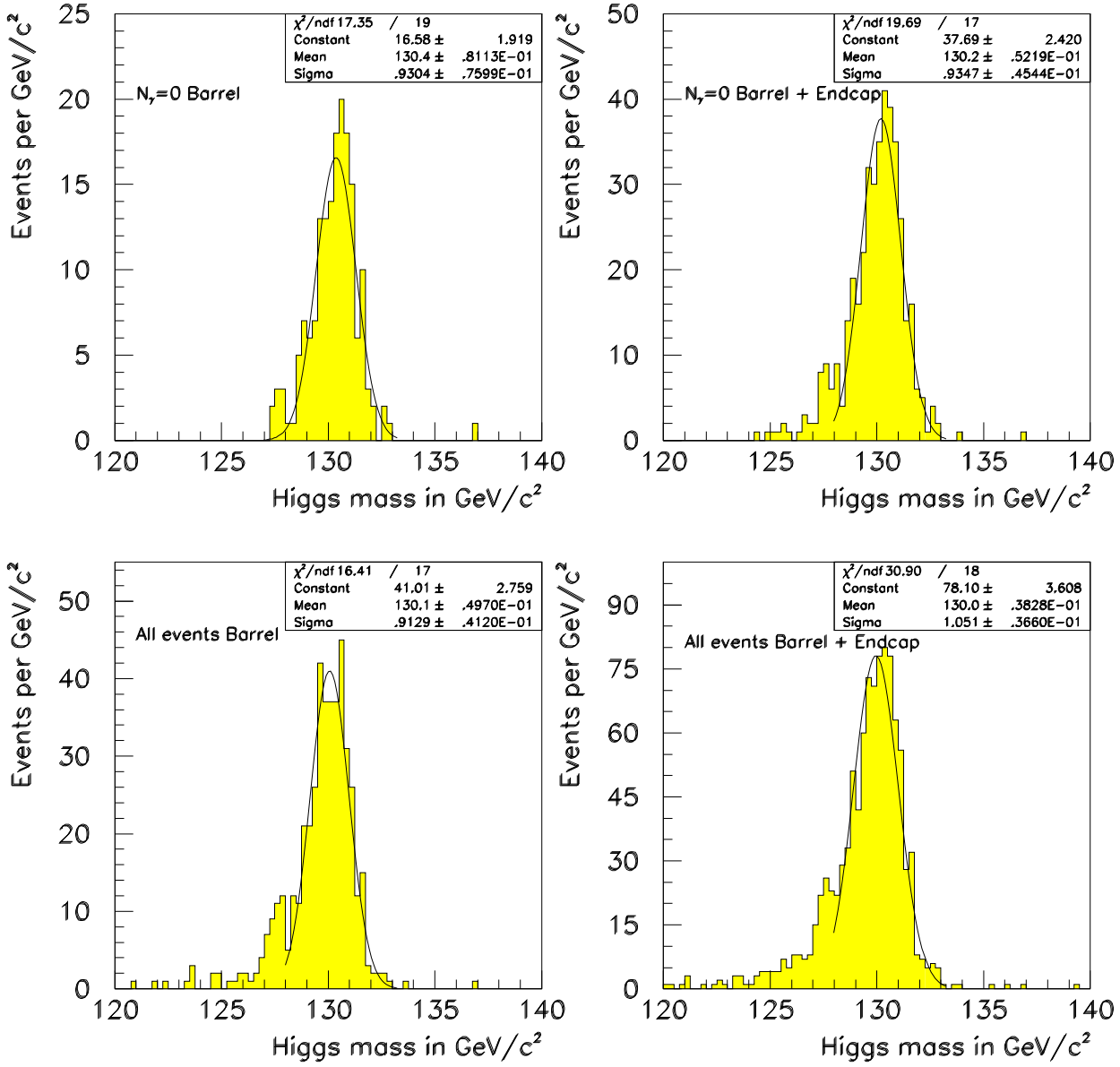

Figure 32: sampling term contribution to the Higgs mass with LKr. Top figures corresponds to events with no inner bremstrahlung, bottom all events.

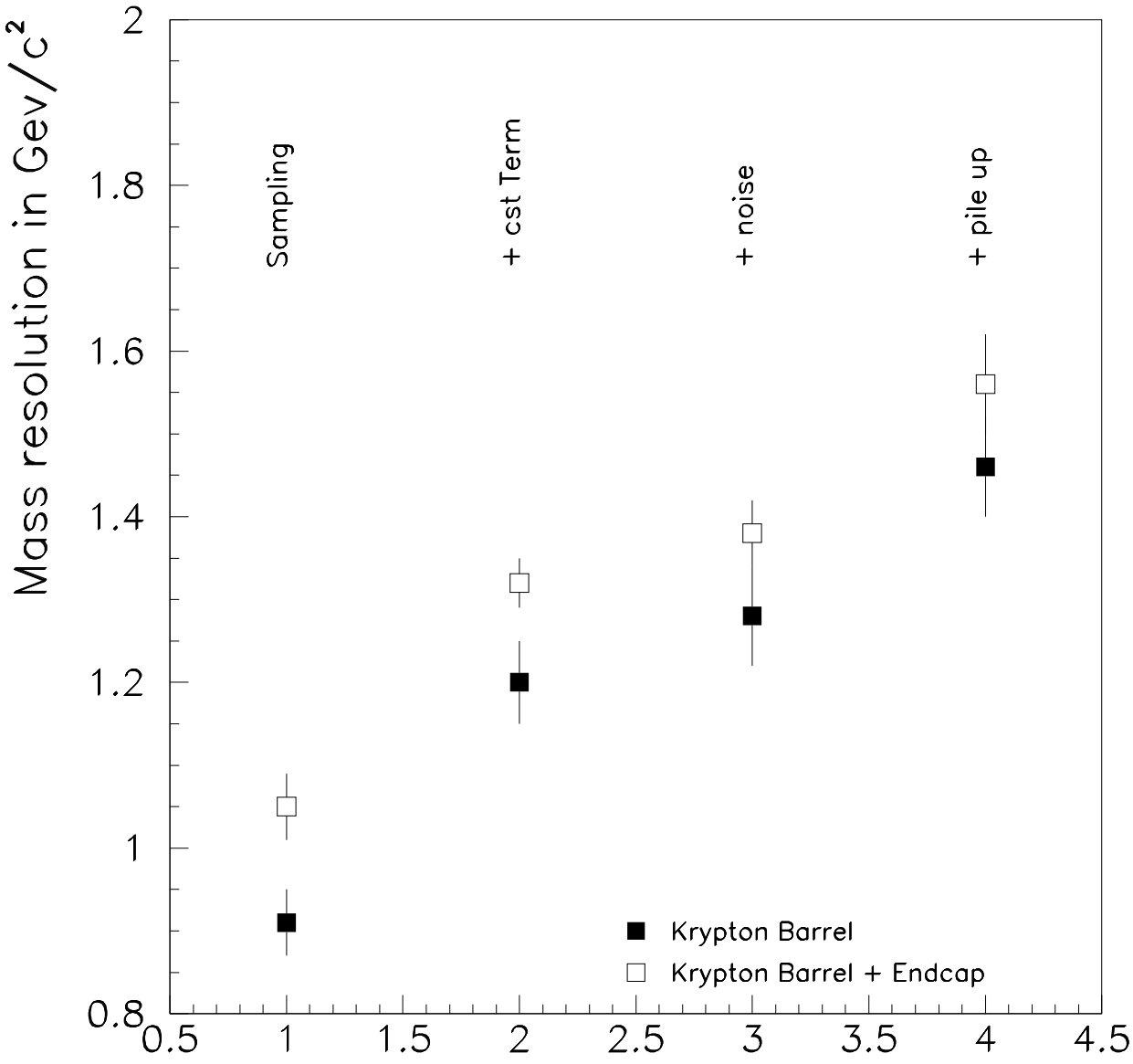

Figure 33: evolution of the Higgs mass by including the various contributions.

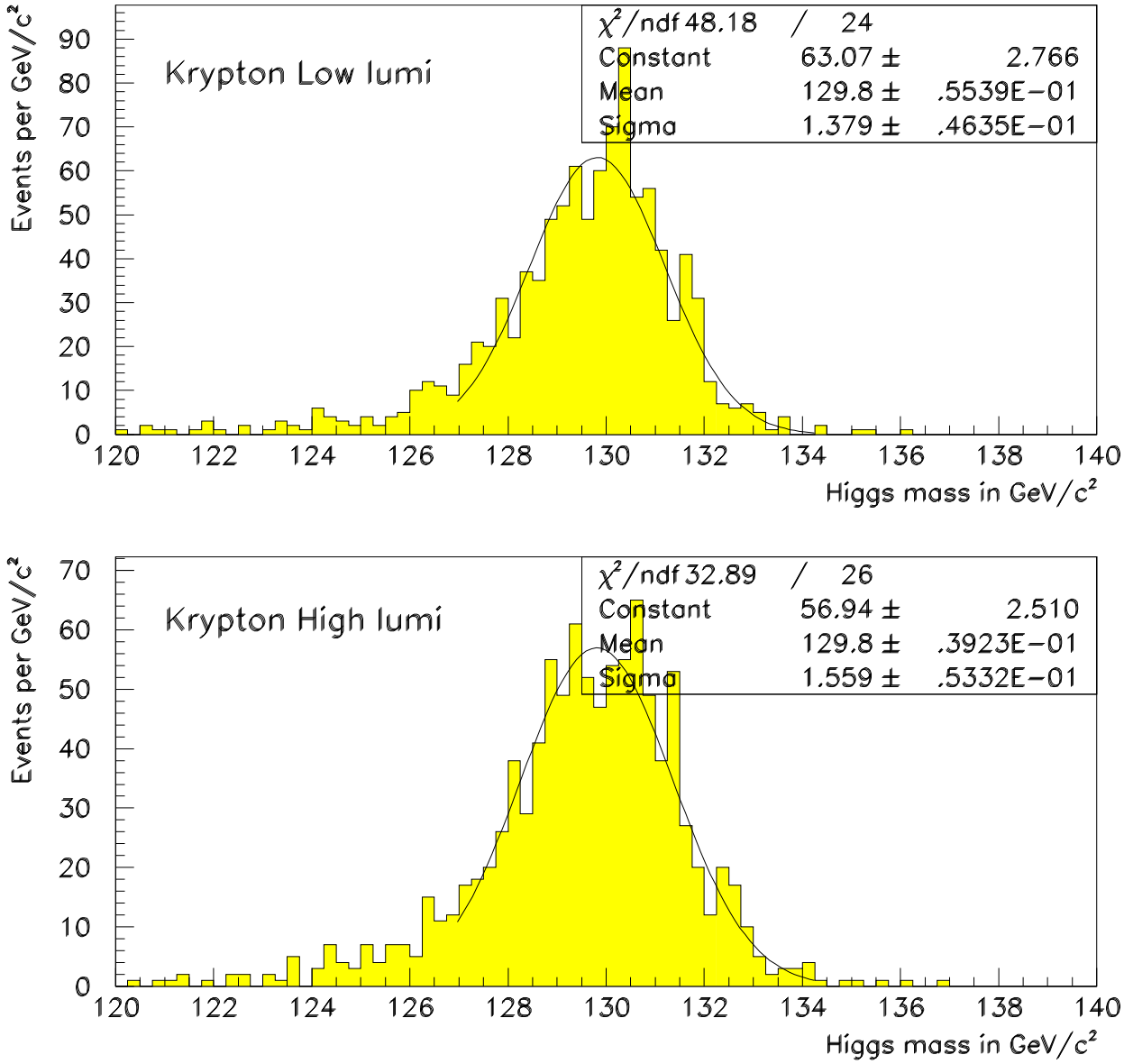

Figure 34: H° mass reconstruction at low and high luminosity in LKr.